Computers and Fluids 215 (2021) 104785

Contents lists available at ScienceDirect

Computers and Fluids

journal homepage: www.elsevier.com/locate/compfluid

A mass-momentum consistent, Volume-of-Fluid method for incompressible flow on staggered grids

T. Arrufat[a], M. Crialesi-Esposito[b], D. Fuster[a], Y. Ling[f], L. Malan[a,c], S. Pal[a], R. Scardovelli[d], G. Tryggvason[e], S. Zaleski[a,*]

[a] Sorbonne Université et CNRS, Institut Jean Le Rond d'Alembert, UMR, Paris 7190, France
[b] CMT-Motores Térmicos, Universitat Politécnica de Valéncia, Camino de Vera, s/n, Edificio 6D, Valencia, Spain
[c] InCFD, Dept. of Mechanical Engineering, University of Cape Town, South Africa
[d] DIN - Lab. di Montecuccolino, Università di Bologna, Bologna I-40136, Italy
[e] Dept. of Mechanical Engineering, Johns Hopkins University, Baltimore, USA
[f] Dept. of Mechanical Engineering, Baylor University, Waco, TX, USA

ARTICLE INFO

Article history:
Received 30 November 2018
Revised 11 August 2020
Accepted 2 November 2020
Available online 19 November 2020

Keywords:
Multiphase flows
Navier-Stokes equations
Volume-of- Fluid
Surface tension
Large density contrast

ABSTRACT

The computation of flows with large density contrasts is notoriously difficult. To alleviate the difficulty we consider a discretization of the Navier-Stokes equation that advects mass and momentum in a consistent manner. Incompressible flow with capillary forces is modeled and the discretization is performed on a staggered grid of Marker and Cell type. The Volume-of-Fluid method is used to track the interface and a Height-Function method is used to compute surface tension. The advection of the volume fraction is performed using either the Lagrangian-Explicit / CIAM (Calcul d'Interface Affine par Morceaux) method or the Weymouth and Yue (WY) Eulerian-Implicit method. The WY method conserves fluid mass to machine accuracy provided incompressibility is satisfied. To improve the stability of these methods momentum fluxes are advected in a manner "consistent" with the volume-fraction fluxes, that is a discontinuity of the momentum is advected at the same speed as a discontinuity of the density. To find the density on the staggered cells on which the velocity is centered, an auxiliary reconstruction of the density is performed. The method is tested for a droplet without surface tension in uniform flow, for a droplet suddenly accelerated in a carrying gas at rest at very large density ratio without viscosity or surface tension, for the Kelvin-Helmholtz instability, for a 3mm-diameter falling raindrop and for an atomizing flow in air-water conditions.

1. Introduction

Multiphase flows abound in nature, but their stable and accurate computation remains elusive in many cases. As a case in point, many numerical methods used for two-phase incompressible flow are strongly unstable for large density contrasts and large Reynolds numbers. Experience with such simulations shows that the presence of surface tension is an aggravating factor. The large density contrasts that are of interest are air/water or gas/liquid-metal, with ρ_l/ρ_g of the order of 10^3 or 10^4. The large density contrasts are a difficulty whether one deals with any of the three major interface advection methods, Level-Set, Volume-of-Fluid (VOF) or Front-Tracking, or with combinations such as CLSVOF. (The term density contrast is preferable to density ratio since it encompasses ratios both much larger than one and much smaller than one.)

Several methods have been used to alleviate the high-density-contrast difficulties. It has been observed by several authors that making the momentum-advection method conservative improves the situation. For incompressible flow, "momentum-conserving" methods have been initially proposed by [1], and by several other authors since [2–7]. These methods have been shown to improve the stability of the numerical results in various situations. In particular, liquid-gas flows with very contrasted densities, as for example in the process of atomization, cause serious problems that are resolved by using momentum-conserving methods. In that case another oft-suggested solution is to increase the number of equa-

* Corresponding author.
E-mail address: zaleski@dalembert.upmc.fr (S. Zaleski).

https://doi.org/10.1016/j.compfluid.2020.104785

tions from the standard four equations to five, six or seven equations, by introducing new field variables in each phase. The addition of one more density ρ_i, momentum $\rho_i \mathbf{u}_i$ or energy variable $\rho_i e_i$ increases the number of equations. The authors of ref [8]. used seven equations, those of [9] used five equations and six equations were used in [10]. The last three references also use a momentum-conserving formulation. Several authors, including some of those cited above, have argued that the difficulty may come from gas velocities of order u_g being mixed with liquid densities of order ρ_l. Both the ρ_l and u_g scales are large and the appearance of an nonphysical $\rho_l u_g^2$ dynamic pressure scale could create numerical pressure fluctuations of the same order and nonphysical pressure spikes, as the one nicely illustrated in [11] in the front part of a suddenly accelerated small droplet. One way of avoiding this nonphysical mixture of liquid and gas quantities is to extrapolate liquid and gas pressure and velocity in the "other" phase, as in the ghost fluid method. This extrapolation strategy was used successfully in [12].

It may be argued that a way to avoid this numerical diffusion of liquid and gas quantities is to advect the volume fraction and the conserved quantities that depend on it (density, momentum and energy) in a consistent manner. In incompressible flow in which we specialize in this paper, it means that the volume fraction and momentum or velocity must be advected in the same way. This is equivalent to request that the discontinuity of the Heaviside function H, marking the phase transition, should be advected at the same speed as the discontinuity in momentum. This can be expressed by the following consistency requirement: if momentum is initially exactly proportional to volume fraction, it should remain so after advection. We call such a method VOF-consistent.

To satisfy this requirement the idea is to solve the advection equation for momentum with the same numerical scheme that is used for the VOF color function. This consistency property minimizes the nonphysical transfer of momentum from one phase to another due to the differences in the numerical schemes used. The consistency is especially important when dealing with fluids with a large density contrast where a small numerical momentum transfer from the dense phase to the light phase results in large numerical errors in the velocity field which in turn creates numerical instabilities.

In this work, we present a modification of the classical momentum-preserving scheme proposed by [1] for the case of a staggered grid and VOF method. The scheme is then not momentum-conserving although it is built by discretization of the momentum conserving formulation of the advection terms, so we rather call it mass-momentum consistent.

The paper is organized as follow: the second section deals with the continuum mechanics formulation for incompressible flow and sharp interfaces. Section 3 describes our numerical method, starting with an overview of already-known methods for spatial discretization, time-stepping, and VOF advection. We continue with the new momentum advection-VOF-consistent method. Section 4 is devoted to tests of the method, followed by a conclusion.

Among the authors, Gretar Tryggvason, Ruben Scardovelli, Yue Ling and Stéphane Zaleski have been involved in the construction of the base of the ParisSimulator VOF and Front-Tracking code that was used to implement and test the ideas in this paper. ParisSimulator is itself based on a Front-Tracking code developed by Gretar Tryggvason, Sadegh Dabiri and Jiacai Lu. Daniel Fuster was involved in the development of the momentum advection method consistent with VOF advection, with help from Tomas Arrufat, Leon Malan and Yue Stanley Ling. The Kelvin-Helmholtz analysis and testing were done by Stéphane Zaleski. The falling raindrop testing and the corresponding figures were done by Tomas Arrufat and Sagar Pal. The large density droplet and shear layer tests were done by Sagar Pal. The atomisation testing was done by Marco Crialesi-Esposito.

2. Navier–Stokes equations with interfaces

We model flows with sharp interfaces defined implicitly by a characteristic function $H(\mathbf{x}, t)$ defined such that fluid 1 corresponds to $H = 1$ and fluid 2 to $H = 0$. The viscosity μ and density ρ are calculated as an average

$$\mu = \mu_1 H + \mu_2 (1 - H)\,, \qquad \rho = \rho_1 H + \rho_2 (1 - H)\,. \tag{1}$$

There is no phase change so the interface, almost always a smooth differentiable surface S, advances at the speed of the flow, that is $V_S = \mathbf{u} \cdot \mathbf{n}$ where $\mathbf{u}$ is the local fluid velocity and $\mathbf{n}$ a unit normal vector perpendicular to the interface. Equivalently the interface motion can be expressed in weak form

$$\partial_t H + \mathbf{u} \cdot \nabla H = 0\,, \tag{2}$$

which expresses the fact that the singularity of H, located on S, moves at velocity $V_S = \mathbf{u} \cdot \mathbf{n}$. For incompressible flows, which we will consider in what follows, we have

$$\nabla \cdot \mathbf{u} = 0\,. \tag{3}$$

The Navier–Stokes equations for incompressible, Newtonian flow with surface tension may conveniently be written in operator form

$$\partial_t (\rho \mathbf{u}) = \mathcal{L}(\rho, \mathbf{u}) - \nabla p \tag{4}$$

where $\mathcal{L} = \mathcal{L}_{\text{conv}} + \mathcal{L}_{\text{diff}} + \mathcal{L}_{\text{cap}} + \mathcal{L}_{\text{ext}}$ so that the operator $\mathcal{L}$ is the sum of advective, diffusive, capillary force and external force terms. The first two terms are

$$\mathcal{L}_{\text{conv}} = -\nabla \cdot (\rho \mathbf{u}\mathbf{u})\,, \qquad \mathcal{L}_{\text{diff}} = \nabla \cdot \mathbf{D}\,, \tag{5}$$

where $\mathbf{D}$ is a stress tensor whose expression for incompressible flow is

$$\mathbf{D} = \mu \left[\nabla \mathbf{u} + (\nabla \mathbf{u})^T \right], \tag{6}$$

where μ is computed from H using (1). The capillary term is

$$\mathcal{L}_{\text{cap}} = \sigma \kappa \delta_S \mathbf{n}\,, \qquad \kappa = 1/R_1 + 1/R_2\,, \tag{7}$$

where σ is the surface tension coefficient, $\mathbf{n}$ is the unit normal perpendicular to the interface, κ is the sum of the principal curvatures and δ_S is a Dirac distribution concentrated on the interface. We assume a constant coefficient σ. Finally $\mathcal{L}_{\text{ext}}$ represents external forces such as gravity.

3. Method

3.1. Spatial discretization

We assume a regular cubic or square grid. This can be easily generalized to rectangular or cuboid grids, and with some efforts to quadtree and octree grids. We also use staggered velocity and pressure grids, as represented in two dimensions in Fig. 1.

The control volume surrounding the pressure p is used for other scalar quantities, such as the density ρ and volume fraction C. The control volumes of the velocity components, u_1 and u_2, and momentum components are shifted respectively half cell horizontally and vertically, with respect to the pressure control volume. The use of staggered control volumes has the advantage of suppressing neutral modes often observed in collocated methods but leads to more complex discretizations (see [13] for a detailed discussion.) This type of staggered representation is easily generalized to three dimensions, and the discrete version of the continuity Eq. (3) is rather compact on such a grid

$$\frac{u_{1;i+1/2,j,k} - u_{1;i-1/2,j,k}}{\Delta x} + \frac{u_{2;i,j+1/2,k} - u_{2;i,j-1/2,k}}{\Delta y}$$

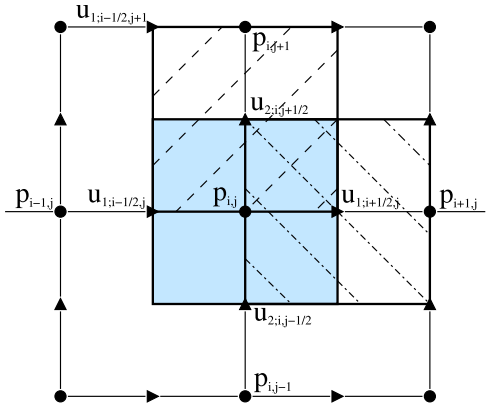

Fig. 1. Representation of the staggered spatial discretization in two dimensions. The pressure $p_{i,j}$ is located at the center of its control volume (light color area); the horizontal velocity component $u_{1;i+1/2,j}$ is stored in the middle of the right edge of the pressure control volume and at the center of its control volume (dash-dotted area); the vertical velocity component $u_{2;i,j+1/2}$ is stored in the middle of the top edge and at the center of its control volume (dashed area).

$$+\frac{u_{3;i,j,k+1/2}-u_{3;i,j,k-1/2}}{\Delta z}=0\,. \tag{8}$$

In what follows, we shall use the subscript $f=m\pm$, with the integer index $m=1,2,3$, to note the face of any control volume located in the positive or negative Cartesian direction m, and $\mathbf{n}_f$ for the unit normal vector of face f pointing outwards of the control volume. On a cubic grid the spatial step is $\Delta x=\Delta y=\Delta z=h$ so the discrete continuity equation becomes

$$\nabla^h\cdot\mathbf{u}=\sum_{m=1}^{3}(u_{m+}+u_{m-})/h=0\,, \tag{9}$$

where $u_f=u_{m\pm}=\mathbf{u}\cdot\mathbf{n}_f$ is the velocity component normal to face f. The discretization of the interface location is performed using a VOF method. VOF methods typically attempt to solve approximately Eq. (2) which involves the Heaviside function H, whose integral in the cell Ω indexed by i,j,k defines the volume fraction $C_{i,j,k}$ from the relation

$$h^3\,C_{i,j,k}=\int_\Omega H\,\mathrm{d}\mathbf{x}\,. \tag{10}$$

$C_{i,j,k}$ represents the fraction of the cell filled with fluid 1, taken to be the reference fluid.

3.2. Time marching

The volume fraction field is updated as

$$C^{n+1}=C^n+\mathcal{L}_{\mathrm{VOF}}(C^n,\mathbf{u}^n\tau/h)\,, \tag{11}$$

where $\mathcal{L}_{VOF}$ represents the operator that updates the Volume of Fluid data given the velocity field. Once volume fraction is updated, the velocity field is updated in a couple of steps. A projection method is first used, in which a provisional velocity field $\mathbf{u}^*$ is computed

$$\begin{aligned}\rho^{n+1}\mathbf{u}^*=\;&\rho^n\mathbf{u}^n+\tau\mathcal{L}^h_{\mathrm{conv}}(\rho^n,\mathbf{u}^n)\\&+\tau\left[\mathcal{L}^h_{\mathrm{diff}}(\mu^n,\mathbf{u}^n)+\mathcal{L}^h_{\mathrm{cap}}(C^{n+1})+\mathcal{L}^h_{\mathrm{ext}}(C^{n+1})\right].\end{aligned} \tag{12}$$

It goes without saying that the above operators depend on the discretization time step τ and spatial step h as well as the fluid parameters. The discussion of the $\mathcal{L}^h_{\mathrm{conv}}$ operator is the main point of this paper. In the second step, the projection step, the pressure gradient force is added to yield the velocity at the new time step

$$\mathbf{u}^{n+1}=\mathbf{u}^*-\frac{\tau}{\rho^{n+1}}\nabla^h p\,. \tag{13}$$

The pressure is determined by the requirement that the velocity at the end of the time step must be divergence free

$$\nabla^h\cdot\mathbf{u}^{n+1}=0\,, \tag{14}$$

which leads to a Poisson-like equation for the pressure

$$\nabla^h\cdot\frac{\tau}{\rho^{n+1}}\nabla^h p=\nabla^h\cdot\mathbf{u}^*\,. \tag{15}$$

3.3. Volume-of-fluid

In this section we detail only the necessary steps to illustrate the momentum advection method based on the VOF method. To simplify the presentation we rescale space and time variables so that the cell volume and the time step are both equal to 1. Any velocity component u becomes $u'=u\tau/h$ and the $C_{i,j,k}$ value is also the measure of the volume of reference fluid in cell i,j,k. At the beginning of any simulation the volume fraction field is initialized with the Vofi library described in [14] and [15]. This allows a highly accurate numerical integration of the measure of fluid volumes.

3.3.1. Normal vector and plane constant determination

The VOF method proceeds in two steps, reconstruction and advection. In the first step we consider a PLIC reconstruction in each cell cut by the interface where the unit normal vector $\mathbf{n}$ is computed with the MYC method described in [13]. We then consider the colinear normal vector $\mathbf{m}$ whose components satisfy the relation $|m_x|+|m_y|+|m_z|=1$. Given the volume $V=C_{i,j,k}$ in cell i,j,k occupied by fluid 1 and the normal $\mathbf{m}$ we consider the family of planes

$$\mathbf{m}\cdot\mathbf{x}=\alpha\,. \tag{16}$$

By changing the value of the plane constant α a different volume of fluid 1 is cut in the cell. The correct value of α is determined by the resolution of a cubic equation [16].

3.3.2. General split-direction advection

The interface reconstruction at time t_n is then used to obtain the position of the interface and the volumes $C_{i,j,k}$ at the next discrete time t_{n+1}. The following discussion of momentum advection is based on two VOF advection methods, Lagrangian Explicit and Weymouth and Yue's schemes. We first describe their common features.

After addition and subtraction of a term proportional to the velocity divergence, Eq. (2) leads to

$$\partial_t H+\nabla\cdot(\mathbf{u}H)=H\,\nabla\cdot\mathbf{u}\,. \tag{17}$$

This equation is integrated in the time step and cell volume

$$C^{n+1}_{i,j,k}-C^n_{i,j,k}=-\sum_{\text{faces f}}F^{(c)}_f+\int_{t_n}^{t_{n+1}}\mathrm{d}t\int_\Omega H\,\nabla\cdot\mathbf{u}\,\mathrm{d}\mathbf{x}\,, \tag{18}$$

where the first term on the right-hand side is the sum over the cell faces f of the fluxes $F^{(c)}_f$ of $(\mathbf{u}H)$. Obviously the "compression" term on the right-hand side disappears for incompressible flow, however it is essential in split-advection methods. In the previous equation the flux $F^{(c)}_f$ is

$$F^{(c)}_f=\int_{t_n}^{t_{n+1}}\mathrm{d}t\int_f u_f(\mathbf{x},t)H(\mathbf{x},t)\,\mathrm{d}\mathbf{x}\,, \tag{19}$$

where $u_f=\mathbf{u}\cdot\mathbf{n}_f$. Once an approximation for the evolution of $(\mathbf{u}H)$ during the time step is chosen, a four-dimensional integral remains to be computed in Eq. (19). The two methods we consider here are directionally split and are also designed to preserve the property $0\le C_{i,j,k}\le 1$ which we call C-bracketing. It is important

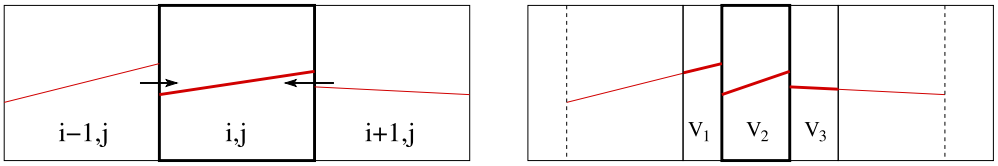

Fig. 2. Formation of the areas V_1, V_2 and V_3 by Lagrangian advection in the horizontal direction: initial reconstruction with the horizontal velocities on the faces of the central cell (left); segments and areas V_i after Lagrangian advection (right). In three dimensions rectangles become cuboids.

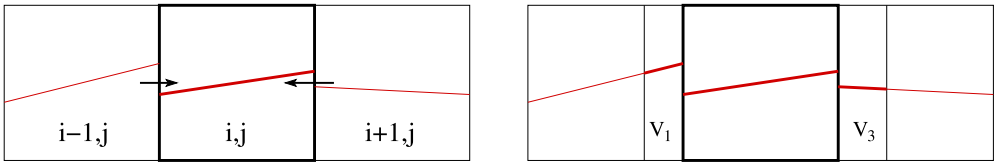

Fig. 3. Eulerian flux representation for advection in the horizontal direction: same initial reconstruction and horizontal velocities of Fig. 2 (left); fluxes, or areas V_1 and V_3, are calculated directly from the interface reconstruction in each cell (right).

to preserve C-bracketing in order to avoid arbitrary addition or removal of mass. Furthermore they do not produce in the bulk of the two fluids deviations from the correct values 0 and 1.

Directional splitting results in the breakdown of equation (18) into three equations

$$C^{n,l+1}_{i,j,k} - C^{n,l}_{i,j,k} = -F^{(c)}_{m-} - F^{(c)}_{m+} + c_m \partial^h_m u_m \,, \tag{20}$$

where the superscript $l = 0, 1, 2$ is the substep index, i.e. $C^{n,0}_{i,j,k} = C^n_{i,j,k}$ and $C^{n,3}_{i,j,k} = C^{n+1}_{i,j,k}$. The face with subscript $m-$ is the "left" face in direction m with $F^{(c)}_{m-} \geq 0$ if the flow is locally from right to left. A similar reasoning applies to the "right" face $m+$. We have also approximated the compression term in (18) by

$$\int_{t_n}^{t_{n+1}} \mathrm{d}t \int_\Omega H \partial_m u_m \mathrm{d}\mathbf{x} \simeq c_m \partial^h_m u_m \,, \tag{21}$$

with no implicit summation rule. In the RHS of (20) and (21) the flux terms $F^{(c)}_f$ and the partial derivative $\partial_m u_m$ must be evaluated with the same discretized velocities. In particular, $\partial^h_m u_m$ is a finite difference or finite volume approximation of the spatial derivative of the mth component of the velocity vector in direction m, and the "compression coefficient" c_m approximates the color fraction. Its exact expression is dependent on the advection method and it preserves the C-bracketing condition. Since the coefficient c_m may not be the same along the three Cartesian directions, the sum $\sum_m c_m \partial^h_m u_m$ is not necessarily vanishing even if the flow is incompressible. After each advection substep (20), the interface is reconstructed with the updated volumes $C^{n,l+1}_{i,j,k}$, then the fluxes $F^{(c)}_f$ are computed for the next substep.

In each substep the velocity field in direction m is usually dependent only on the spatial component x_m, $u_m(x_m)$. This approximation ensures that the fluid areas fluxing across a cell side are rectangular in two dimensions, as shown in Figs. 2 and 3. The multi-dimensionality of the flow is considered in unsplit methods, where the fluxing areas are described by more complex polygons [17].

3.3.3. Lagrangian explicit advection

The Lagrangian Explicit / CIAM method refers to a specific type of split advection and it is most naturally explained as a Lagrangian transport of the Heaviside function [18,19]. The velocity field is linearly interpolated between the face velocities u_{m-} on the left and u_{m+} on the right, so that $u_m(x_m) = -u_{m-}(1 - x_m) + u_{m+} x_m$, with the origin of x_m on the left face. The equation of motion $dx_m/dt = u_m(x_m)$ is integrated with a first-order in time, explicit $u_m(x^n_m)$ approximation, to get in rescaled variables

$$x^{n+1}_m = -u_{m-} + (1 + u_{m+} + u_{m-})\, x^n_m \,. \tag{22}$$

This transformation gives the position of advected points as a function of the original position and compresses distances along direction m by a factor $(1 + u_{m+} + u_{m-})$. Points over faces and linear interface are advected in the same way, and in the two-dimensional case of Fig. 2 the advection substep results in the three contributions V_1, V_2 and V_3 to the central cell. The intermediate value of the color function in the central cell will be given by the sum of these three contributions.

There is a correspondence between the geometrical interpretation of the Lagrangian Explicit advection and the definition (19) of $F^{(c)}_f$. For example, for the central cell of Fig. 2 the flux on the left face is from left to right, since $u_{1;i-1/2,j} > 0$. Then with $m = 1$ and $f = 1-$, we have $V_1 = -F^{(c)}_{1-} > 0$ and $u_{1-} = \mathbf{u} \cdot \mathbf{n}_{1-} < 0$. The final expression of the substep is

$$C^{n,l+1}_{i,j,k} = C^{n,l}_{i,j,k}(1 + u_{m+} + u_{m-}) - F^{(c)}_{m-} - F^{(c)}_{m+} \,, \tag{23}$$

which shows that the approximation of the derivative is $\partial^h_m u_m = u_{m+} + u_{m-}$ and the compression coefficient is

$$c_m = C^{n,l}_{i,j,k}. \tag{24}$$

In order to remove spurious asymmetries in the flow it is important to change the order of split advections at each timestep. Then the compression coefficient in the horizontal advection, $m = 1$, can be associated to the first substep, $l = 0$, in timestep n, and to the last substep, $l = 2$, in the next timestep. The sequence of three Lagrangian substeps (20) does not result in volume conservation

$$C^{n+1}_{i,j,k} - C^n_{i,j,k} = -\sum_{\text{faces f}} F^{(c)}_f + \sum_{m=1}^{3} c_m \left(u_{m+} + u_{m-}\right). \tag{25}$$

While the flux terms cancel upon integration over the domain, the sum of the compressive terms does not vanish since c_m changes at each substep l.

3.3.4. Weymouth and Yue's advection

The (WY) split advection is exactly mass-conserving [20]. In this method the compression coefficient is independent of direction m, so that $c_m = c$, and is defined as

$$c = H\left(C^n_{i,j,k} - 1/2\right) \tag{26}$$

where H is a one-dimensional Heaviside function, that is $c = 0$ if $C^n_{i,j,k} < 1/2$ and $c = 1$ if $C^n_{i,j,k} \geq 1/2$. The fluxes $F^{(c)}_f$ are also defined differently. The reference phase fluxed through the left face in direction $m = 1$ is equal to the volume fraction in a cuboid of width

$u_{i-1/2,j,k}$ adjacent to the left face $f = 1-$. This fluxed volume corresponds to "Eulerian Implicit" (EI) advection in the terminology of [19] and is represented in 2D by the area V_1 of Fig. 3. Using these definitions, Weymouth and Yue were able to show that the final result obeys C-bracketing [20].

This split advection scheme conserves volume at machine accuracy. Indeed the summation of three substeps (20) results in

$$C^{n+1}_{i,j,k} - C^{n}_{i,j,k} = -\sum_{\text{faces f}} F^{(c)}_f + c\sum_{m=1}^{3} \partial^h_m u_m. \tag{27}$$

Since $\sum_{m=1}^{3} \partial^h_m u_m = \sum_{m=1}^{3} (u_{m+} + u_{m-})$ is the finite-volume expression for $\nabla \cdot \mathbf{u}$, it disappears and mass is conserved at the accuracy with which condition (3) is satisfied.

3.3.5. Clipping

The algorithm that has been coded involves a number of additional steps designed to avoid unwanted effects of arithmetic floating point round-off error. The most important one is clipping: at the end of each directional advection, the values of $C_{i,j,k}$ are reset so that C_{ijk} is set to 0 if $C_{ijk} < \epsilon_c$ or to 1 if $C_{ijk} > 1 - \epsilon_c$. When there is no surface tension the choice $\epsilon_c = 10^{-12}$ works well. Otherwise $\epsilon_c = 10^{-8}$ gives more stable results with smoother interface shapes. This stronger clipping is a necessity for some simulations with WY, as we observe that WY produces many more "wisps", i.e. cells with tiny values of $1 - C_{i,j,k}$ inside fluid 1 or $C_{i,j,k}$ inside fluid 2. We have not yet been able to determine the origin of this need for a more forceful clipping with WY, but it could be related to the fact that the CIAM method has a geometrical interpretation, while WY is intrinsically algebraic in nature.

3.4. Momentum-advection methods

3.4.1. Advection of a generic conserved quantity

Consider the advection of a generic *conserved* quantity ϕ by a continuous velocity field

$$\partial_t \phi + \nabla \cdot (\phi\, \mathbf{u}) = 0. \tag{28}$$

We assume that ϕ is smoothly varying except on the interface where it may be discontinuous. Indeed finding a correct scheme for the advection of this discontinuity, at the same speed as the advection of the volume fraction, is the goal of the present study. The smoothness of the advected quantity away from the interface is verified for the density ρ, the momentum $\rho\mathbf{u}$ or the internal energy ρe. We first integrate (28) in time

$$\phi^{n+1}_{i,j,k} - \phi^{n}_{i,j,k} = -\sum_{\text{faces f}} F^{(\phi)}_f\,. \tag{29}$$

The sum on the right-hand side is the sum over faces f of cell i, j, k of the fluxes $F^{(\phi)}_f$ of ϕ, which are defined in the same way as the color function fluxes $F^{(c)}_f$ in (19)

$$F^{(\phi)}_f = \int_{t_n}^{t_{n+1}} \mathrm{d}t \int_f u_f(\mathbf{x},t)\, \phi(\mathbf{x},t)\, \mathrm{d}\mathbf{x}. \tag{30}$$

In order to "extract" the discontinuity we introduce the characteristic function $H(\mathbf{x},t)$

$$F^{(\phi)}_f = \int_{t_n}^{t_{n+1}} \mathrm{d}t \int_f [u_f\, H\, \phi + u_f\,(1-H)\,\phi]\, \mathrm{d}\mathbf{x}\,, \tag{31}$$

and rewrite it as

$$F^{(\phi)}_f = \bar{\phi}_1 \int_{t_n}^{t_{n+1}} \mathrm{d}t \int_f u_f\, H\, \mathrm{d}\mathbf{x} + \bar{\phi}_2 \int_{t_n}^{t_{n+1}} \mathrm{d}t \int_f u_f\,(1-H)\, \mathrm{d}\mathbf{x}\,, \tag{32}$$

where the face averages $\bar{\phi}_s$, $s = 1, 2$, are

$$\bar{\phi}_s = \frac{\int_{t_n}^{t_{n+1}} \mathrm{d}t \int_f \phi\, u_f\, H_s \mathrm{d}\mathbf{x}}{\int_{t_n}^{t_{n+1}} \mathrm{d}t \int_f u_f\, H_s\, \mathrm{d}\mathbf{x}}\,, \tag{33}$$

and $H_1 = H$, $H_2 = 1 - H$. Expression (32) can be written in terms of the fluxes $F^{(c)}_f$ and $F^{(1-c)}_f$, this second one being obtained by replacing H with $1 - H$ in (19)

$$F^{(\phi)}_f = \bar{\phi}_1\, F^{(c)}_f + \bar{\phi}_2\, F^{(1-c)}_f\,. \tag{34}$$

3.4.2. Cloning the tracers

When a cell is cut by the interface, and the field ϕ is not smooth, it becomes difficult to estimate the integrals in (32). A possibility is to define two new fields ϕ_1 and ϕ_2, with $\phi_s = \phi$ inside phase s, then

$$\phi = H\,\phi_1 + (1-H)\,\phi_2\,. \tag{35}$$

This is more costly in memory usage but simplifies considerably the computation of the averages in (32). The two equations (2) and (28) are now replaced by three equations, the same volume fraction Eq. (2) and

$$\partial_t \phi_1 + \nabla \cdot (\phi_1 \mathbf{u}) = 0\,, \qquad \partial_t \phi_2 + \nabla \cdot (\phi_2 \mathbf{u}) = 0\,. \tag{36}$$

The three Eqs. (2) and (36) now imply (28). The addition of a pair of "cloned" variables to deal with large density contrasts is similar to the methods used for the resolution of the momentum and energy equations for compressible flow. For example Saurel and Abgrall used two density, momentum and energy variables in their seven-equations model [8], while Allaire, Clerc and Kokh use two density variables in their five-equations model [9]. The addition of a cloned tracer variable in incompressible isothermal flow was also implemented by Popinet in the "Basilisk" code [21].

3.4.3. Advection of the density field

The density $\rho(\mathbf{x},t)$ obeys (28) with $\phi = \rho$. Moreover we consider a divergence-free velocity field, with constant density in each phase. We can extract the density trivially from the integrals (33) to obtain *exactly* $\bar{\rho}_s = \rho_s$. The flux of ρ is then

$$F^{(\rho)}_f = \rho_1 F^{(c)}_f + \rho_2 F^{(1-c)}_f. \tag{37}$$

Using this flux definition for ρ, and any VOF method for the fluxes of the color function, one obtains a conservative method for ρ, since eq. (29) evolves ρ as a difference of fluxes. Thus the total mass is conserved. However this result is not consistent with the advection of the color function in the CIAM case, as CIAM does not conserve volumes exactly (see (25)). As a result the advection of ρ is not consistent with the advection of C.

This paradox may be resolved if one notices that the compression term is missing in (28). For consistency the compression term should be kept, and the advection equation for a conserved quantity becomes

$$\partial_t \phi + \nabla \cdot (\phi\, \mathbf{u}) = \phi\, \nabla \cdot \mathbf{u}. \tag{38}$$

It is then possible to define the evolution of ϕ through a sequence of directionally-split operations which are equivalent to the operations performed on the color function

$$\phi^{n,l+1}_{i,j,k} - \phi^{n,l}_{i,j,k} = -F^{(\phi)}_{m-} - F^{(\phi)}_{m+} + \left(\tilde{\phi}^m_1 c^{(1)}_m + \tilde{\phi}^m_2 c^{(2)}_m\right) \partial^h_m u_m \tag{39}$$

where $F^{(\phi)}_{m\pm}$ are defined in (34), the cell averages $\tilde{\phi}^m_s$ are

$$\tilde{\phi}^m_s = \frac{\int_{t_n}^{t_{n+1}} \mathrm{d}t \int_\Omega \phi H_s \partial^h_m u_m\, \mathrm{d}\mathbf{x}}{\int_{t_n}^{t_{n+1}} \mathrm{d}t \int_\Omega H_s \partial^h_m u_m\, \mathrm{d}\mathbf{x}}\,, \tag{40}$$

and $c^{(1)}_m = c_m$ is the compression coefficient of the VOF advection, while $c^{(2)}_m = 1 - c_m$ is that of the symmetric color fraction $1 - C$. Specifically for ρ this gives

$$\rho^{n,l+1}_{i,j,k} - \rho^{n,l}_{i,j,k} = -F^{(\rho)}_{m-} - F^{(\rho)}_{m+} + C^{(\rho)}_m\,, \tag{41}$$

where the fluxes are given by (37) and the compression term is

$$C_m^{(\rho)} = \left(\rho_1 c_m^{(1)} + \rho_2 c_m^{(2)}\right) \partial_m^h u_m \tag{42}$$

with no implicit summation on m and $c_m^{(s)}$ given by (24) or (26). For the WY method, the compression terms eventually cancel out and mass is conserved at the same accuracy as the discrete incompressibility condition $\sum_{m=1}^{3} \partial_m^h u_m = 0$ is verified.

3.4.4. Momentum advection: basic expressions

For momentum advection we consider the transport of the scalar quantities $\phi = \rho u_q$, where $q = 1, 2, 3$ is the component index. With definition (33), we obtain for the face weighted averages $\tilde{\phi}_s = \overline{\rho u_q}_s$ the expression

$$\overline{\rho u_q}_s = \rho_s \bar{u}_{q,s} \tag{43}$$

where

$$\bar{u}_{q,s} = \frac{\int_{t_n}^{t_{n+1}} \mathrm{d}t \int_f u_q u_f H_s \,\mathrm{d}\mathbf{x}}{\int_{t_n}^{t_{n+1}} \mathrm{d}t \int_f u_f H_s \,\mathrm{d}\mathbf{x}} \tag{44}$$

We term $\bar{u}_{q,s}$ the "advected interpolated velocity" and explain below how it is computed. Thus the evolution of the momentum is given by

$$(\rho u_q)_{i,j,k}^{n,l+1} - (\rho u_q)_{i,j,k}^{n,l} = -F_{m-}^{(\rho u)} - F_{m+}^{(\rho u)} + \left(\rho_1 \tilde{u}_{q,1}^m c_m^{(1)} + \rho_2 \tilde{u}_{q,2}^m c_m^{(2)}\right) \partial_m^h u_m \tag{45}$$

where

$$F_f^{(\rho u)} = \rho_1 \, \bar{u}_{q,1} \, F_f^{(c)} + \rho_2 \, \bar{u}_{q,2} \, F_f^{(1-c)}\,, \tag{46}$$

and the "central interpolated velocity", corresponding to the averages $\tilde{\phi}_s^m$ of (40), are

$$\tilde{u}_{q,s}^m = \frac{\int_{t_n}^{t_{n+1}} \mathrm{d}t \int_\Omega u_q \, H_s \, \partial_m^h u_m \,\mathrm{d}\mathbf{x}}{\int_{t_n}^{t_{n+1}} \mathrm{d}t \int_\Omega H_s \, \partial_m^h u_m \,\mathrm{d}\mathbf{x}}. \tag{47}$$

From now on we omit the superscript m for $\tilde{u}_q^m$ to avoid too complex notations. Notice that "cloning" the advected velocities $\bar{u}_{q,1}$ and $\bar{u}_{q,2}$ would make it easier to advect a velocity field with a jump on the interface. However in viscous flow without phase change the velocity is continuous on the interface, and to avoid an excessively complicated method we approximate the velocity field as continuous and we choose $\bar{u}_q = \bar{u}_{q,1} = \bar{u}_{q,2}$ for the "advected interpolated velocity" and $\tilde{u}_q = \tilde{u}_{q,1} = \tilde{u}_{q,2}$ for the "central interpolated velocity". An important simplification is then

$$F_f^{(\rho u)} = \bar{u}_q F_f^{(\rho)} \tag{48}$$

(which is the central equation in this development) and thus

$$(\rho u_q)_{i,j,k}^{n,l+1} - (\rho u_q)_{i,j,k}^{n,l} = -\bar{u}_q F_{m-}^{(\rho)} - \bar{u}_q F_{m+}^{(\rho)} + \tilde{u}_q C_m^{(\rho)}, \tag{49}$$

where the density fluxes are defined in (37) and the compression term $C^{(\rho)}$ in (42). In the above expression the face-weighted average velocities $\bar{u}_q$ are defined using (44) on the corresponding left face $m-$ or right face $m+$. It is important to note that up to this point the weighted averages $\bar{u}_q$ and $\tilde{u}_q$ have been defined but the method in which they are estimated in the numerical method will be given only in what follows.

If we combine the scheme above with the CIAM scheme, the compression coefficient in the volume fraction advection from (24) is $C^{n,l}$, and for the central interpolated velocity we take $\tilde{u}_q = u_q^{n,l}$. The compression term in (49) does not cancel out when the final momentum is computed after three directionally-split advections and the result is not exactly conservative. On the other hand with the WY scheme, the compression coefficient in the volume fraction advection from (26) is c, that is independent of direction m and (42) becomes

$$C_m^{(\rho)} = \left(\rho_1 c + \rho_2 (1-c)\right) \partial_m^h u_m\,. \tag{50}$$

Since there is no bracketing on the velocity components, we take $\tilde{u}_q = u_q^n$ which is independent on the substep l. Provided the velocity field is incompressible, that is $\sum_{m=1}^{3} \partial_m^h u_m = 0$, after the three split advections (49) one obtains a cancellation of the compression terms and

$$(\rho u_q)_{i,j,k}^{n,3} - (\rho u_q)_{i,j,k}^{n} = -\sum_{\text{faces f}} \bar{u}_q F_f^{(\rho)}. \tag{51}$$

The momentum transport coupled with WY advection is thus exactly conservative. The advected interpolated velocity $\bar{u}_q$ and the velocity u_f normal to face f are discussed in the next section.

3.4.5. Momentum advection: interpolations and flux limiters

The momentum Eq. (49) can be approximated either 1) in the bulk of the phases or 2) in the neighborhood of the interface. In the first case the expression simplifies considerably since both the density and the color fraction are constant and the spurious compression terms cancel out

$$u_q^{n,3} - u_q^n = -\sum_{\text{faces f}} \bar{u}_q u_f. \tag{52}$$

We distinguish an "advecting" velocity $u_f = \mathbf{u} \cdot \mathbf{n}_f$ and an "advected velocity" component $\bar{u}_{q,f}$, involving an average over face f. Both velocity components require an interpolation from their position in the staggered grid to where they are needed. Thus the scheme in the bulk is

$$u_q^{n,3} - u_q^n = -\sum_{\text{faces f}} \bar{u}_q^{(\text{advected})} u_f^{(\text{advecting})}\,, \tag{53}$$

while near the interface is

$$(\rho u_q)^{n,3} - (\rho u_q)^n = -\sum_{\text{faces f}} \bar{u}_q^{(\text{advected})} F_f^{(\rho)} + \sum_{m=1}^{3} \tilde{u}_q C_m^{(\rho)}\,. \tag{54}$$

Momentum advection in our model is described by these two equations which are solved on a cubic grid with a finite-volume method. In the previous sections we have derived a new expression for the momentum fluxes and the compression term, i.e. the RHS of (54), that is consistent with the volume fraction advection.

To estimate the advecting velocities $u_f^{(\text{advecting})}$ we use a centered scheme. The staggered 2D grid of Fig. 1 has the same variables arrangement that is found in 3D on a plane perpendicular to the z-axis and through the pressure point $p_{i,j,k}$. To illustrate the procedure we consider a face perpendicular to the horizontal direction 1, in particular $f = 1-$. There are two cases. In the first case the advected component is not aligned with the face normal, this corresponds to $q = 2$. The u_2 control volume in Fig. 1 is centered on $i, j+1/2, k$, and face $f = 1-$ is then centered on $i-1/2, j+1/2, k$. The advecting velocity $u_{1-}^{(\text{advecting})}$ is not given on this point and has to be interpolated

$$u_{1;i-1/2,j+1/2,k}^{(\text{advecting})} = \frac{1}{2}\left(u_{1;i-1/2,j,k} + u_{1;i-1/2,j+1,k}\right). \tag{55}$$

In the second case the advected component is aligned with the face normal, this corresponds to $q = 1$. The u_1 control volume in Fig. 1 is centered on $i+1/2, j, k$ and face $f = 1-$ is then centered on i, j, k. The interpolation is now

$$u_{1;i,j,k}^{(\text{advecting})} = \frac{1}{2}\left(u_{1;i-1/2,j,k} + u_{1;i+1/2,j,k}\right). \tag{56}$$

Now we turn to the interpolation of the *advected* velocity $\bar{u}_q$ in (54). The interpolants we use in this case are one-dimensional and operate on the velocities u_q, on the center of their control volume,

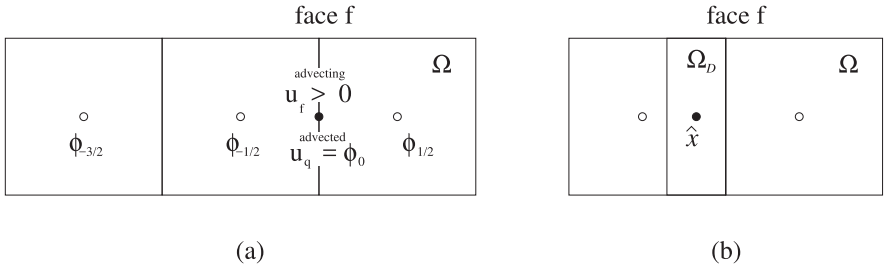

Fig. 4. The reference control volume Ω for the advected velocity component $\phi = u_q$ is shown. A horizontal advection is here considered and both the advecting velocity u_f and the advected velocity require an interpolation for their value on the left face $f = 1-$: (a) the value $\bar{u}_q = \phi_0$ (full circle) is interpolated (see Appendix A) from the values $\phi = u_q$ on the nodes (open circles); (b) a more sophisticated interpolation predicts the value $\phi(\hat{x})$ where $\hat{x}$ is at the center of the "donating" region Ω_D (see Appendix A).

that are regularly spaced on a segment aligned with the direction of the advection, that is perpendicular to face f. We still consider an advection along the horizontal direction 1. In Fig. 4, with the lighter notation $\phi = u_q$, we need to interpolate the advected velocity on the left face of the reference control volume Ω. For the advected velocity u_1 and the advecting velocity (56) on face $f = 1-$ the correspondence with the ϕ values in Fig. 4 is

$$\phi_{-3/2} = u_{1;i-3/2,j,k}, \quad \phi_{-1/2} = u_{1;i-1/2,j,k}, \quad \phi_{1/2} = u_{1;i+1/2,j,k}, \quad \cdots \tag{57}$$

while for the advected velocity u_2 and the advecting velocity (55) is

$$\phi_{-3/2} = u_{2;i-2,j+1/2,k}, \quad \phi_{-1/2} = u_{2;i-1,j+1/2,k}, \quad \phi_{1/2} = u_{2;i,j+1/2,k}, \quad \cdots \tag{58}$$

The extension of these results to an advection along the other two directions $q = 2, 3$ follows easily. We need to predict ϕ_0 on face $f = 1-$ in Fig. 4 to serve as an approximation of $\bar{u}_q$ given in (44). We consider an interpolation function f that computes this value as a function of the four nearest points, and in an upwind manner based on the sign of the *advecting* velocity u_f

$$\phi_0 = f\left(\phi_{-3/2}, \phi_{-1/2}, \phi_{1/2}, \phi_{3/2}, \mathrm{sign}(u_f)\right). \tag{59}$$

In this study we have extensively tested two kinds of interpolations:

1. a scheme that uses a QUICK third-order interpolant in the bulk, away from the interface and a simple first-order upwind flux near the interface. We call this scheme QUICK-UW;
2. a scheme that uses a Superbee slope limiter [22] for the flux in the bulk and a more complex Superbee limiter tuned to a shifted interpolation point near the interface. We naturally call this scheme "Superbee".

The details of the two schemes are given in Appendix A.

3.4.6. VOF-consistent momentum advection on staggered grids

In order to apply the above method on the staggered grid, we need the color fraction data in the velocity control volumes. At the start of the velocity advection operations, summarized by the operator $\mathcal{L}^h_{\mathrm{conv}}$, each velocity control volume overlaps two pressure/VOF control volumes, for example $\Omega_{i+1/2,j}$ overlaps $\Omega_{i,j}$ and $\Omega_{i+1,j}$ in the 2D case of Fig. 5. An estimate of the shifted volume fraction $C_{i+1/2,j}$ in $\Omega_{i+1/2,j}$ is then obtained by performing the usual reconstructions in $\Omega_{i,j}$ and $\Omega_{i+1,j}$ and adding the two half-fractions. The following operations are then performed at each time step and are summarized in Algorithm 1:

1. Reconstruction of the interface at time t_n from the data C^n, and computation of the shifted fraction of Fig. 5 to obtain the "shifted" data C^n_q and ρ^n_q in the staggered control volumes ($q = 1, 2, 3$ is the component index), for example ρ_1 in $\Omega_{i+1/2,j,k}$ for the horizontal momentum component $\rho_1 u_1$.

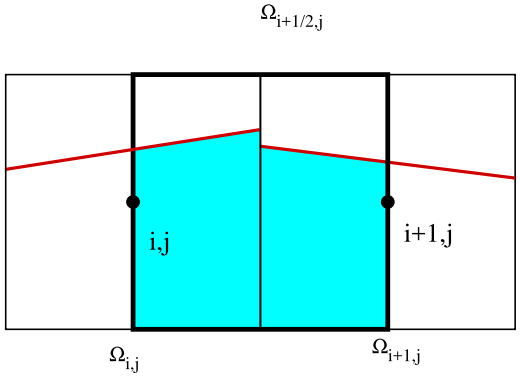

Fig. 5. Computation of the shifted volume fractions from the half-fractions.

Algorithm 1 Summary of the algorithm for the momentum and VOF time step.

Reconstruct interface from volume fractions C^n
for each component q **do**
  Compute "shifted" volume fraction $C^{n,0}_q$ in the staggered control volumes
  Compute density $\rho^{n,0}_q$ (Eq. 1)
  Compute momentum component $(\rho_q u_q)^{n,0}$
end for
for each substep l **do**
  for each component q **do**
    Momentum advection in the x_l direction to compute $(\rho_q u_q)^{n,l+1}$(Eq. 49)
    (the x_l coordinate direction changes with the time step)
    VOF advection of "shifted" C_q in the x_l direction to compute$C^{n,l+1}_q$
    Compute density $\rho^{n,l+1}_q$ (Eq. 1)
    Update velocity component $u^{n,l+1}_q = (\rho_q u_q)^{n,l+1}/\rho^{n,l+1}_q$
  end for
  VOF advection of C in pressure control volumes in the x_l directionto compute
  $C^{n,l+1}$
end for

2. Computation of the three momentum components $(\rho_q u_q)^n$ at time t_n.
3. Advection of the three momentum components along one coordinate direction, say x direction, using (49) to obtain the updated momentum components $(\rho_q u_q)^{n,1}$ after the first substep.
4. Advection with the VOF method of the "shifted" volume fraction data C^n_q of the staggered control volumes along the x direction to obtain the updated volume fractions $C^{n,1}_q$ and from (1) the densities $\rho^{n,1}_q$ after the first substep.

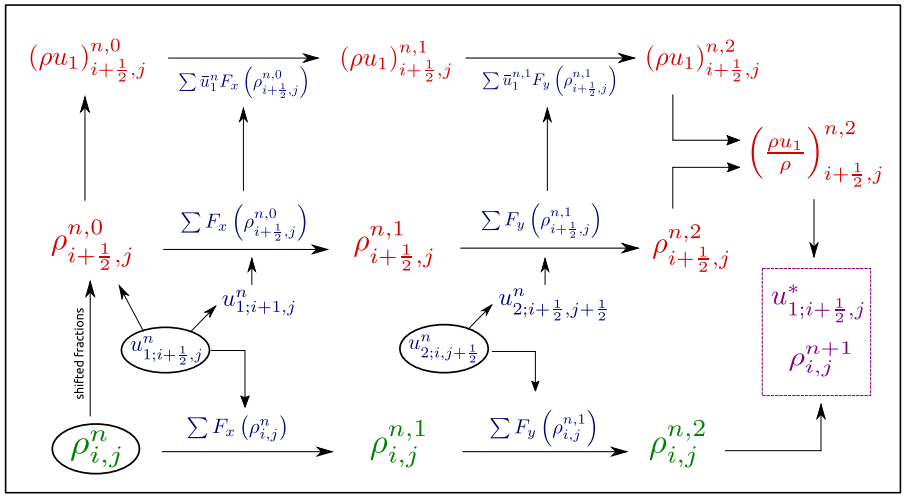

Fig. 6. Diagram of the time step. For simplicitythe 2D case is represented for the density on the grid i, j and for the horizontal velocity u_1 on the staggered grid $i+1/2, j$. The evolution of the velocity component u_2 on the staggered grid $i, j+1/2$ is similar. The initial variables ρ^n, u_1^n, u_2^n are inside the ellipses. The interpolated "advecting" components u_1 and u_2 have superscript n. The shifted density $\rho^{n.0}$ is constructed with the shifted fractions of C to initialize the momentum component $(\rho u_1)^{n.0}$. The first split advection is along the x direction to variables with superscript $n,1$, the second one is along the y direction to variables with superscript $n,2$. The updated density is $\rho^{n.2} = \rho^{n+1}$ while the horizontal velocity $u_1^{n.2} = u_1^*$ enters the RHS of the Poisson-like equation (15).

5. Extraction of the provisional velocity components $u_q^{n,1}$ after the first substep, $u_q^{n,1} = (\rho_q u_q)^{n,1}/\rho_q^{n,1}$.
6. Repeat the previous operations for momentum components, shifted volume fractions and densities, and velocity components for the next two substeps with split advections along the y and z directions. Eventually obtain $(\rho_q u_q)^{n+1} = (\rho_q u_q)^{n,3}$ and $\tilde{\rho}_q^{n+1} = \rho_q^{n,3}$. At each time step, the sequence x, y, z is permuted.
7. In parallel, computation of $C^{n+1} = C^{n,3}$ on the pressure control volumes using the VOF method.

The interface reconstruction, the computation of volume fraction fluxes and the interpolation of "advected" and "advecting" velocity components have been detailed in the previous sections. We remark that the advected velocity components u_q are updated at each substep, while the advecting velocities u_f are interpolated from the initial velocity field $\mathbf{u}^n$ at time t_n. The shifted fractions of Fig. 5 are computed by the same routine that is computing the Eulerian fluxes V_1 and V_3 of Fig. 3.

The three momentum components $(\rho_q u_q)^{n+1}$ at the beginning of next time step t_{n+1} require the computation of the three "shifted" volume fractions C_q^{n+1} and densities ρ_q^{n+1} starting from C^{n+1}. However, these densities ρ_q^{n+1} are different from the densities $\tilde{\rho}_q^{n+1} = \rho_q^{n,3}$ computed in the previous time step by directly advecting the "shifted" volume fractions C_q^n. The reason for this difference is that the linear reconstruction is approximate and it is not even continuous on the boundary of its control volume. As a matter of facts, at each substep we have four slightly different interface reconstructions. This implies that momentum is not conserved between two time steps. We note that attempting to always use only the three sets C_q^n and evolve them by the VOF method on the staggered cells would maintain conservation but result in the three staggered grids evolving independently of each other and eventually diverging. A diagram of the whole scheme is presented in Fig. 6.

3.5. Description of the other time-split terms

The other time-split terms in Eq. (12) and in the projection step (13) are solved in a standard centered way. The density on the faces of the central cells $\Omega_{i,j,k}$ is estimated using a simple average $\rho_{i+1/2,j,k} = (\rho_{i,j,k} + \rho_{i+1,j,k})/2$. Although this is less accurate and consistent than the usage of the densities ρ_q, computed from the shifted fractions as described above, the simple average is used both for simplicity and because tests have shown that the usage of ρ_q leads to less stable simulations.

The velocities in the diffusion term are introduced in an explicit way. Although this requires small time steps of the order $\rho h^2/\mu$, the capillary restriction on time steps is usually even smaller, being of order $\tau = (\rho h^3/\sigma)^{1/2}$. The two restrictions become of the same order when $h \sim l_{\mu\sigma}$, where $l_{\mu\sigma} = \mu^2/(\sigma\rho)$ is the length at which the viscous and capillary terms balance. For water, this length is of the order of 10 nanometers, and grids of that size are not used in the flows we consider. However, should the velocities be treated in an implicit manner, we do not believe this would change the conclusions of this paper.

Surface tension is computed using the Continuous Surface Force method proposed by [23], together with an estimate of the curvature through the computation of height functions, in a manner that closely follows the method of [24]. The external forces in equation (12) are only gravity and are computed in a trivial manner with $\frac{1}{\rho^{n+1}}\mathcal{L}_{ext} = \mathbf{g}$, where gravity $\mathbf{g}$ is a constant.

4. Testing and validation

4.1. Consistent cylinder advection

An elementary test of our method, that mostly verifies that the coding has been performed correctly, considers a uniform planar velocity field $u_1 = u_2 = 1.6 \times 10^{-2}$ and a droplet of density $\rho_l = 10^9$ in gas at density $\rho_g = 1$ with a CFL number of $0.0256\sqrt{2}$. Viscosity and surface tension are set to zero in this first test. The number of grid point in the diameter of the droplet is $D/h = 3.2$. The unit domain is discretized on a 16×16 grid. The droplet shapes that result are shown on the left of Fig. 7. The irregularities seen in the advected droplet are due to the roughness of the VOF approximation at such low resolutions. We repeat the test with conditions close to air/water: now viscosities are $\mu_l = 0.1$, $\mu_g = 0.002$ and densities are $\rho_g = 1$, $\rho_l = 10^3$, while there is still no surface tension. We get identical results: a viscosity contrast will not generate numerical instabilities on a uniform velocity field, as shown on the right of Fig. 7.

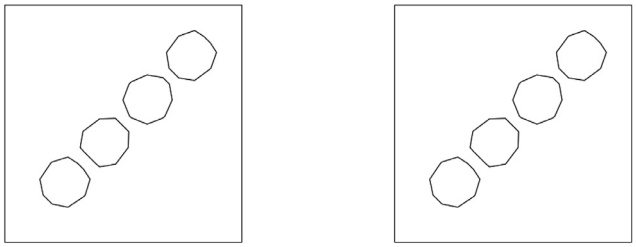

Fig. 7. Large-density-ratio droplet in a uniform velocity field: a droplet with $D/h = 3.2$ grid points per diameter is advected in 3D in the plane $z = 0$ (see text); left: density ratio 10^9 without viscosity, right: density ratio 10^3 with viscosity.

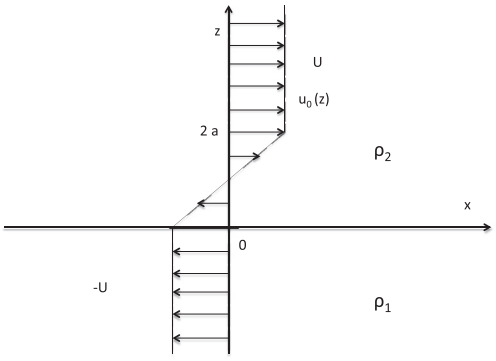

Fig. 8. Base velocity profile.

4.2. Kelvin helmholtz instability

The Kelvin-Helmholtz instability arises between unequal velocity fluid streams. It is closely related to the issues addressed in the current paper since it arises in many of the flows for which the current method is designed, such as atomisation. Moreover, the Kelvin-Helmholtz instability is particularly strong on a vortex sheet, since (as we show in the next section) it has for an infinitely thin sheet a divergent growth rate as the wavenumber goes to infinity. Compounding the issue, the baroclinic term of the vorticity equation leads for unequal densities to the creation or strengthening of a vortex sheet on the interface. In previous papers some of us have studied the Kelvin-Helmholtz instability in viscous flows with surface tension [25–27].

We focus here, in contrast to these earlier papers, on the inviscid, no surface tension case. Indeed we want to focus on the new discretization of the advection terms. Moreover the inviscid, no surface-tension case is a kind of "worst-case scenario" without the stabilizing effects of viscosity and capillarity.

4.2.1. Problem setup

The simplest setup is that of a vortex sheet, for which the growth rate is given by

$$\omega_i = \frac{2\sqrt{r}}{r+1} kU \tag{60}$$

where $r = \rho_g/\rho_l$. This vortex-sheet setup is however leading to an ill-posed problem since for increasing k, exponentially large amplitudes are predicted at finite time. It is thus desirable to regularize the growth rate by having a boundary layer. The theory of the inviscid Kelvin-Helmholtz instability with a boundary layer is summarized in Appendix B. We consider two kinds of boundary layers: (i) a boundary layer in the liquid phase, (ii) a boundary layer in the gas phase. Both cases may be represented by the sketch in Fig. 8. The resulting growth rate is a function of the dimensionless number $\kappa = 2ak$. The dimensionless growth rate $\Omega_i = \omega_i a/U$ is plotted on Fig. 9 for three different density ratios, and for both cases (i) and (ii) above. It is seen that the growth-rate curve has a maximum at $\Omega_{i,max}$ for $\kappa = \kappa_{\max}$ and vanishes above the threshold κ_c. As the density contrast increases, the behavior is different depending on the case. (i) For a boundary layer in the liquid, the interfacial problem becomes in the limit $r \to 0$ a free-surface problem and the growth rate goes to a limit. (ii) On the other hand for a boundary layer in the gas, the maximum growth rate and the corresponding maximum reduced wavenumber $\kappa_{\max}$ both tend to zero and

$$\Omega_{i,max} \sim \sqrt{r}, \quad \kappa_{max} \sim \sqrt{r}. \tag{61}$$

We initialize all simulations with one perturbed wavelength in the computational domain, so that $k = 2\pi/L_x$ and we choose parameters so that $k = k_{\max}$. Then for $\kappa_{\max} = 2ak_{\max} = 4\pi a/L_x$ the number of points in the boundary layer is $2a/h = L_x\kappa_{\max}/(2\pi h) = n_x\kappa_{\max}/(2\pi)$ where $n_x = L_x/h$ is the number of grid points in the horizontal. In the $r = 0.01$ case with the boundary layer in the gas, we have $\kappa_{\max} \simeq 1.2$ and thus $a \simeq 0.2L_x$ for k near $k_{\max}$ and $2a/h \sim n_x/5$. We initialize the simulation with the following method. We use the solution obtained in Appendix B for the mode corresponding to $\kappa_{\max} = 2ak_{\max}$. The modes computed in Appendix B are extending to $\pm\infty$ in the vertical, so a sufficiently large box in the vertical has to be selected. We thus use an $L_x \times L_z$ domain with $L_z = 2L_x$. The error on the boundary at $z = \pm L_z/2$ is of order $e^{-kL_z/2} = e^{-2\pi} \simeq 2\,10^{-3}$.

We choose the boundary layer thickness and the initial amplitudes of the perturbations such that the excited wavelength corresponds to the box size. Moreover it is important to notice that wavenumbers are quantized in the box so that $k_n \pi n/L_x$. Since $2\kappa_{\max} > \kappa_c$ as can easily be seen on Fig. 9 all the quantized modes above the first one are stable. This would not be the case if a narrower boundary layer were used. In the other limit, for a vortex sheet setup ($a = 0$), all modes are unstable in stark contrast with the above situation.

The flow field $u_0(x, z, t = 0), w_0(x, z, t = 0)$ in the initial condition is initialized using a discrete stream function formulation. The motivation for this is the desire to avoid a projection of the velocity field at the first time step. Indeed, less careful initialization methods may start with a velocity field that has a large localized divergence. One may wonder how the pressure gradient in the projection step rearranges this velocity field, possibly inadvertently transferring energy to modes other than the theoretically selected one. As a result, the theory in Appendix B computes the stream function ψ at initial time. The code computes the finite differences

$$u_0 = \partial_z^h \psi, \qquad w_0 = -\partial_x^h \psi \tag{62}$$

allowing the resulting field to be discretely divergence free. This means that it obeys (14) at machine accuracy. The unperturbed interface, according to the theory, is located in the mid-horizontal-plane $z = 0$ of the (1×2) box thus exactly at the boundary of two "centered" C_{ijk}-cells. However it is possible and interesting to shift vertically by $\Delta z = h/2$ the origin of the coordinate system to locate the interface in the *middle* of a row of "centered" C_{ijk}-cells. In addition in what follows we uniformly set $L_x = 1$.

4.2.2. Results for boundary layer in the liquid phase

In order to verify that the numerical scheme is consistent with the theory, we first compute the growth rate for case (i). In what follows we first show results for the WY/QUICK-UW combination of VOF and momentum advection methods, and both for the classical method and with the VOF-momentum-consistent method. The case for $a = \kappa_{\max} L_x/(4\pi) = 0.095$ is shown in Fig. 10. The numerical results are plotted in two manners. The "amplitude growth" plots follow the logarithm of the amplitude of the Fourier mode

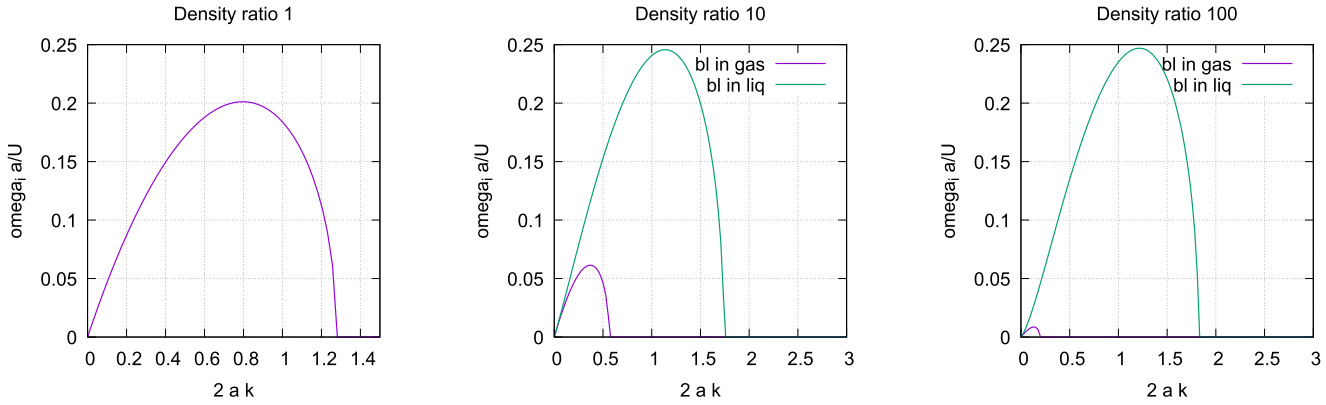

Fig. 9. The reduced growth rate as a function of the dimensionless wavenumber.

of wavenumber $k = 2\pi$. This has the effect of filtering any contribution of the other modes (the other modes should not grow according to the theory but could still appear because of numerical approximations). The second plot is the "maximum velocity" plot which follows the logarithm of the max norm of the vertical velocity $w_{\max}(t) = ||w||_\infty$. The maximum velocity corresponds to a superposition of the amplitude of all the modes.

We first show the results for $n_x = 64$ which corresponds to $2a/h \simeq 13$ points in the boundary layer with $\Delta z = 0$. The initial interface perturbation amplitude is $A_h = 10^{-4}$ and that of the velocity is $w_{\max}(0) = |\omega A_h|$ (see Appendix for the definition of A_h). The results for amplitude growth are good, showing exponential growth over nearly three orders of magnitude. However the results for the maximum velocity growth show a glitch, with an nonphysical jump in the velocity in the case of the VOF-consistent method. The glitch is created by small scale vortical structures with large wavenumber near the interface. These structures have a small amplitude and are overtaken by the physical growth of the $k = 2\pi/L_x$ mode after some time, with a recovery of the predicted growth rate. In the case of the non-consistent method the glitch is not seen. If now one places the interface in the middle of the cell the glitch disappears.

As expected, the results become worse when the boundary layer contains a smaller number of grid points. For $n_x = 16$ exponential growth is still observed (Fig. 11b) over nearly three orders of magnitude, but with a growth rate approximately 13% smaller than the theoretical one. For $n_x = 8$ there is not much more than a single grid point in the boundary layer, and the growth rate is approximately 50% smaller (Fig. 12a). Finally the $n_x = 8$ case for $\Delta z = 0$ and with the maximum velocity plot is a kind of worst case scenario. However even in that case the code does not diverge (Fig. 12b), and the growth is eventually damped, which despite the disagreement with theory has the advantage of stabilizing the computation.

4.2.3. Results for boundary layer in the gas phase

We now turn to the case where the boundary layer is in the gas phase. For $r = 100$ the maximum growth rate is obtained for $\kappa_{\max} \simeq 0.143$. We now have a reduction by approximately one order of magnitude of $\kappa_{\max}$ and thus also of a and a/h. Now if L_x is the wavelength with maximum growth, the boundary layer thickness must be $a \simeq 0.011$ and the number of grid points in the boundary layer is much smaller than with the boundary layer in the liquid phase, with $a/h \simeq 0.02 n_x$. Indeed for $n_x = 64$ there is only about one point in the boundary layer. It is interesting to notice that if a larger a were used, the gas boundary layer would become stable, and the only growth would result from the spurious numerical growth of modes which in theory should be stable. With $n_x = 512$ there are about 12 points in the boundary layer. The computation is beset by numerical instabilities that lead to the blowup of the simulation, so we use $\Delta z = h/2$ and the CIAM/Superbee method, as the later is more stable. The results are shown in Fig. 13a. Both the consistent and non-consistent method give identical results at short times, close to the theory, but with less accuracy than when the boundary layer is in the liquid phase. At times around $t = 0.7$ a small scale instability starts appearing in the maximum velocity graph (Fig. 13b) and eventually causes the demise of the simulation.

With a smaller number of points, $n_x = 256$ and $a/h = 6$ points in the boundary layer, the results shown in Fig. 14 display again a spurious growth due to a small scale numerical instability for the non-consistent method around $t = 2.5$.

4.2.4. Results for the vortex sheet case

In the vortex sheet case, there is no boundary layer thickness and there are no remaining length scales from the theoretical (continuum) point of view. Various ratios of wavelength to grid size are plotted on Fig. 15. In this case the results are best for $\lambda/h = 8$ and adding more grid points does not improve the results, except for a short interval of time for $\lambda/h = 64$. The theoretical growth rate is indeed obtained for $n_x = 64$ in a small interval of time for $t < 0.25$. For the least resolved case, the highest grid (Nyquist) frequency corresponding to $\lambda/h = 2$, there is no amplification but rather damping, indicating that numerical dissipation defeats the instability at this wavenumber. This indicates that the mechanism that makes the computation diverge in other cases is not represented by the Kelvin-Helmholtz instability at near-Nyquist wavenumbers $kh = \mathcal{O}(1)$. The latter is true at least in the current setup of this instability. Other setups, with for example different Δz, or with interfaces not aligned on the grid, may give different results.

However, it is still possible that the excitation of relatively large wavenumbers by the initial perturbation could explain the uncontrolled growth of numerical instabilities at large density contrasts. To test this hypothesis, we plot on Fig. 16 the numerical growth of $||v||_\infty$ compared to the theoretical growth for $r = 1$, for a fixed value of λ/h. We first describe the case $\Delta z = h/2$. It is seen on Fig. 16 that the growth rate is larger than the theoretical one even for $r = 1$. This is explained by the leakage of energy from the initial $k = k_1$ mode into modes with larger $k = k_n$ that have a larger growth rate as expressed by (60). Also on Fig. 16 is seen that for smaller values of r, the growth rates are reduced. However, for the consistent method, a stronger reduction is achieved. It is obvious that this reduction is still very far from being as strong as that predicted by the theory, which would yield a growth rate $\omega_i \sim 10^{-5}$ for the smallest r. We now turn to the case $\Delta z = 0$. In this case,

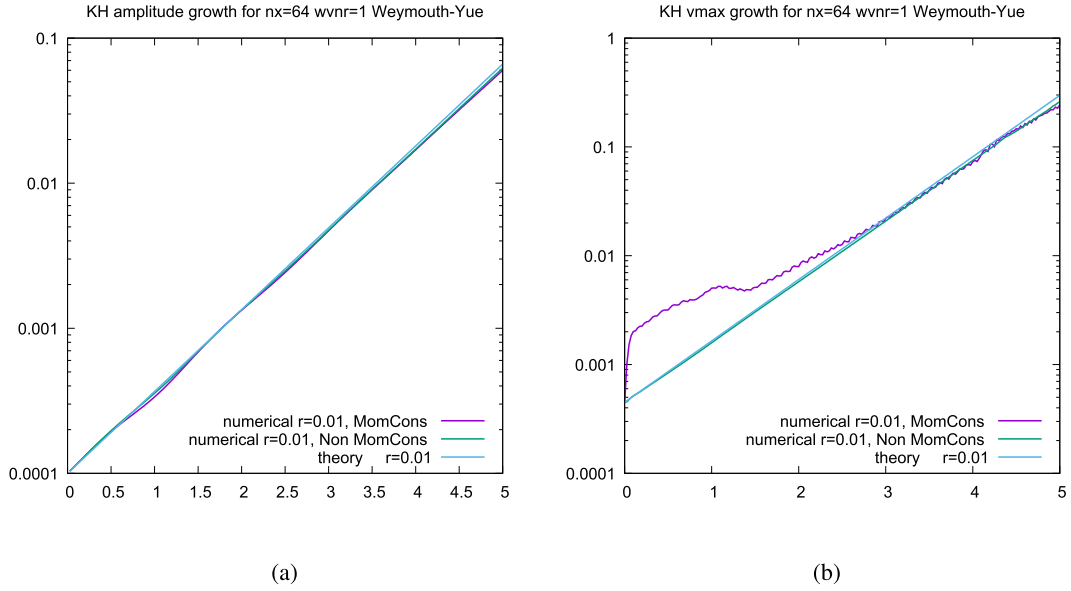

Fig. 10. Comparison of the theoretical and numerical growth for a boundary layer in the liquid as a function of time with $n_x = 64$ grid points, 13 points in the boundary layer and shift $\Delta z = 0$ (see text): (a) amplitude plot; (b) maximum velocity plot. The signal "jumps" by one order of magnitude for the consistent method (nicknamed "MomCons") while it remains close to the theory for the non-consistent method.

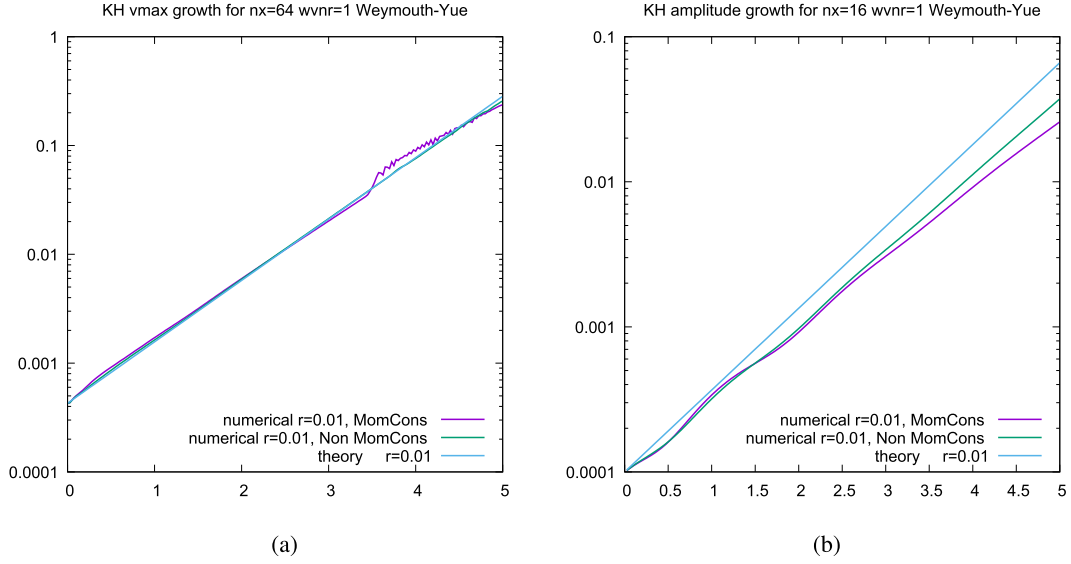

Fig. 11. Comparison of the theoretical and numerical growth for a boundary layer in the liquid as a function of time: (a) maximum velocity plot for shift $\Delta z = h/2$ and other parameters as in Fig. 10. The nonphysical "jump" for the consistent method disappears; (b) amplitude plot for a smaller number of grid points $n_x = 16$ (with $2a/h = 3$ points in the boundary layer) and shift $\Delta z = h/2$.

as shown on Fig. 17, the situation is reversed: the non-consistent method grows much more slowly than the consistent method. For $r = 1$ the growth of the non-consistent method, after a fast initial transient, is altogether stopped. For $r = 10^{-10}$ a super-fast increase is seen. This fast increase is made smaller when the clipping value (see Section 3.3.5) ϵ_c is increased and is made even faster when ϵ_c is decreased. In the set of tests described in this section ϵ_c was set to 10^{-8}.

4.3. Sudden acceleration of a cylinder at large density contrast

A test that is often included in studies of momentum-conserving or mass-momentum-consistent methods [2–7] and other methods designed to improve the stability of two-phase flow computations [28] is to initialize a droplet of very high density at velocity $\mathbf{u}_l(\mathbf{x}) = U_0\mathbf{e}$ with the other, lighter fluid, at rest, so that $\mathbf{u}_g(\mathbf{x}) = 0$. Surface tension and viscosity are not present as in the previous test, the only difference being the discontinuity of the initial velocity on the interface, which amounts to a vortex sheet on the surface of the cylinder. After the first time step, the projection method (13) adds a dipole potential flow so that $\mathbf{u}_g = \tau\nabla p/\rho_g$ in the gas around the droplet, identical to the dipole flow around a solid object and with a slightly different velocity U of the droplet. Indeed, the dipole flow absorbs some of the initial momentum of the liquid in the gas, and results in a reduction from U_0 to U of the droplet velocity during the first time step, similar to the momentum transfer after the traversal of the droplet by a shock wave. This velocity shift, which is estimated in [29], is small, of order $r = \rho_g/\rho_l$. There are at least three ways to explain the perturbations created on the interface.

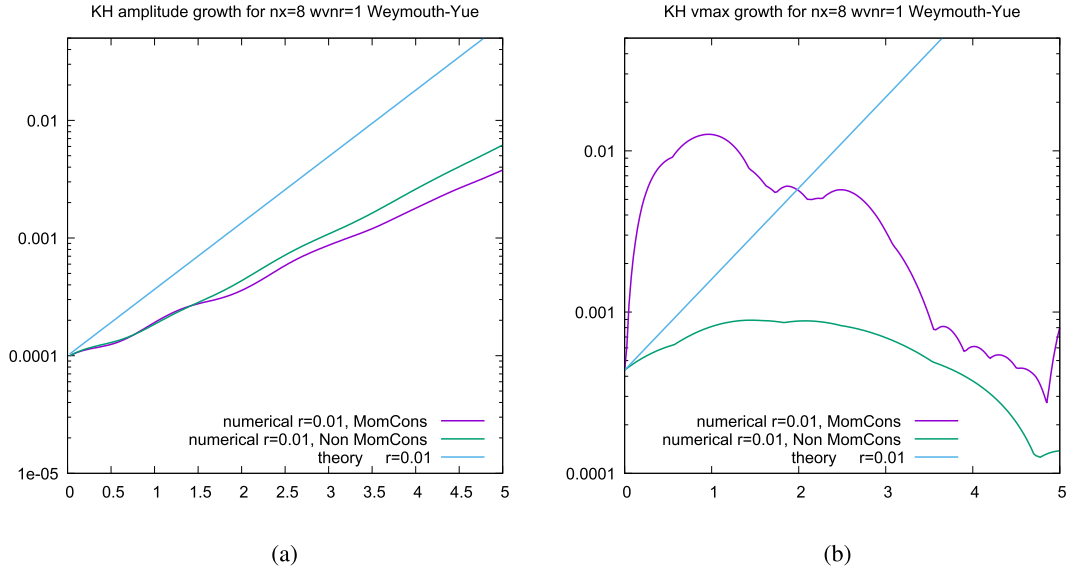

Fig. 12. Comparison of the theoretical and numerical growth for a boundary layer in the liquid as a function of time with $n_x = 8$ grid points (with $2a/h = 1.5$ points in the boundary layer): (a) amplitude plot with shift $\Delta z = h/2$; (b) maximum velocity plot in the "worst case" scenario with shift $\Delta z = 0$. The nonphysical "glitch" for the consistent method is marked, but both methods eventually result in the damping of the perturbation.

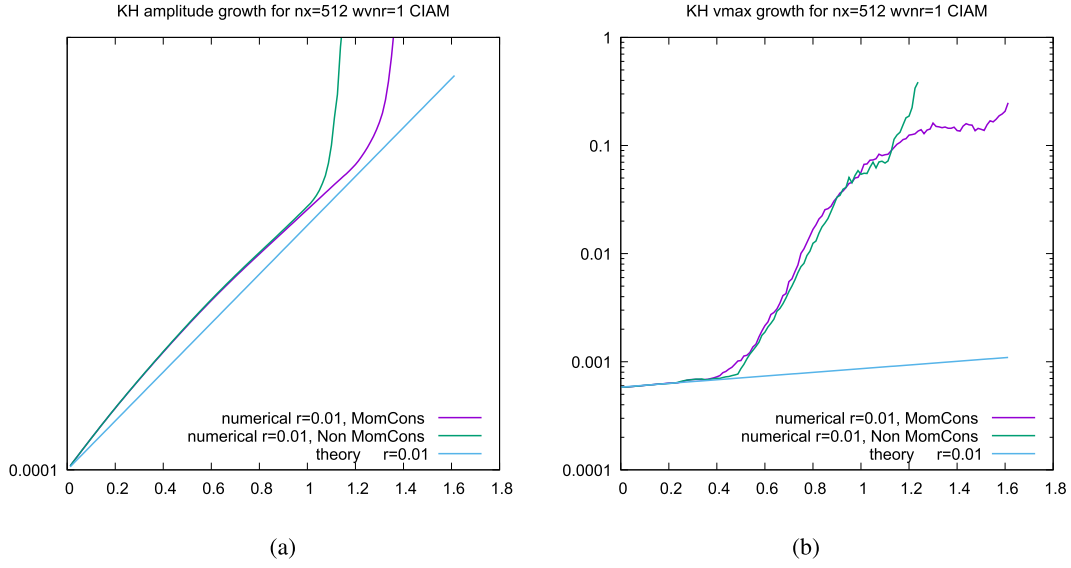

Fig. 13. Comparison of the theoretical and numerical growth for a boundary layer in the gas as a function of time with $n_x = 512$ grid points, $a/h \simeq 12$ points in the boundary layer, shift $\Delta z = h/2$ and $U\tau/h = 0.32$: (a) amplitude plot. The simulation follows approximately the theory but blows up after time $t \simeq 1$, with a faster blow up for the non-consistent method; (b) maximum velocity plot. The rapid growth starting at $t \simeq 0.7$ is due to the appearance of small structures that are stable in the linear theory but not in the numerics.

First, as seen in the previous section and in the Appendix, a vortex sheet is unstable with respect to the Kelvin-Helmholtz instability. The perturbation amplitude $A(t)$ grows exponentially as $A(t) \sim A(0)\exp(\omega_i t)$ with ω_i given by Eq. (60). In the limit of small r the growth rate becomes small, on the order of $\sqrt{r}$. Since the maximum wavenumber on the grid is π/h, an estimate of the growth rate of the small wavelength instabilities is $\pi UN\sqrt{r}/D$, where N is the number of grid points per diameter. After advection by a droplet diameter, the elapsed time is $\Delta t = D/U$. For typical orders of magnitude in the literature of $r = 10^{-6}$ and $N = 32$ the amplitude growth would be

$$\exp(\omega_{i,\max}\Delta t) = \exp\left(\pi N\sqrt{r}\right) = \exp(0.032\pi) = 1.1058\ldots \quad (63)$$

which means the amplitude should grow by 10% after advection by one diameter and by $\sqrt{e}$ after advection by 5 diameters.

Second, beyond the linear growth stage of the Kelvin-Helmholtz instability, there is a self-similar, non-linear growth stage for which dimensional analysis implies that $A(t) \sim \sqrt{r}Ut$ [30]. By this argument also the perturbation of the cylinder should remain small, of order $A(\Delta t) \sim D\sqrt{r}$, after advection by a droplet diameter.

Third, physical deformation is expected from the spatial pressure variation induced by the dipole gas flow. This variation involves a larger pressure at the aft and fore stagnation points and a lower pressure along the equator of the droplet [31]. The resulting integrated stress is of order $\rho_g U^2$ resulting in the growth of the droplet deformation as $A(t) \sim rU^2t^2/D$ and after advection by a droplet diameter as $A(\Delta t) \sim rD$. This growth is observed experimentally [32] and results in an elliptically shaped (mode 2) drop, albeit of much smaller amplitude than

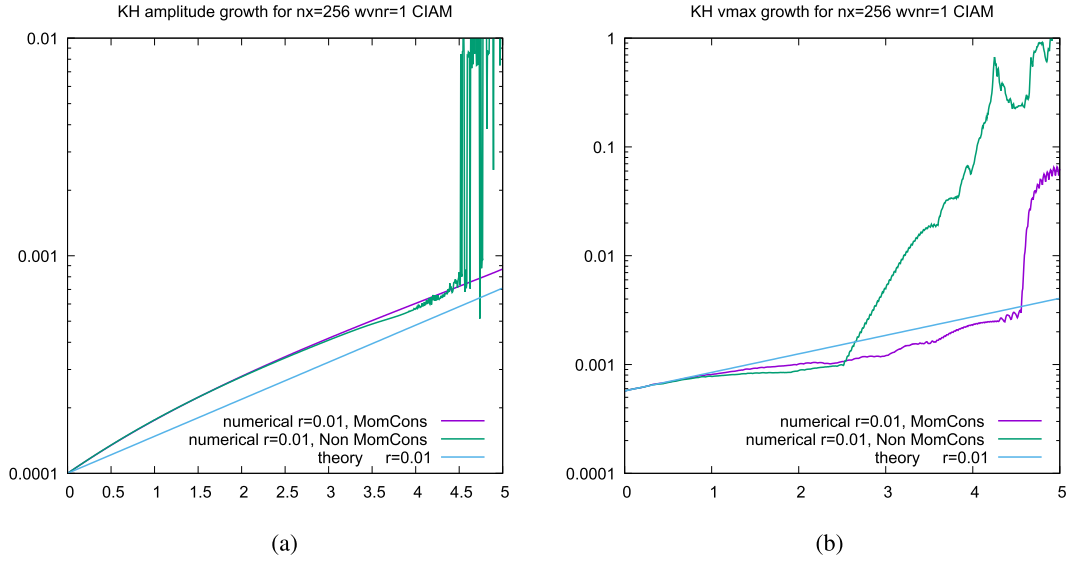

Fig. 14. Comparison of the theoretical and numerical growth for a boundary layer in the gas as a function of time with $n_x = 256$ grid points, $a/h \simeq 6$ points in the boundary layer, shift $\Delta z = h/2$ and $U\tau/h = 0.08$: (a) amplitude plot; (b) maximum velocity plot.

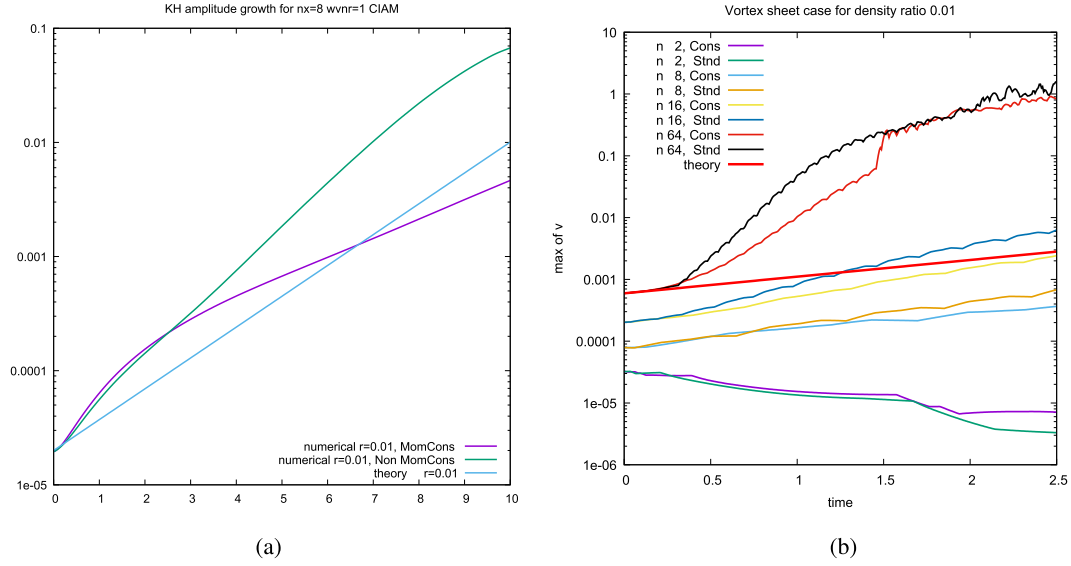

Fig. 15. Kelvin-Helmholtz instability in the vortex sheet case with density ratio $r = 0.01$: (a) amplitude plot for $n_x = 8$; (b) maximum velocity plot. The number n indicates the ratio λ/h of wavelength to grid size, "Cons" stands for consistent method and "Stnd" for non-consistent method.

the two former Kelvin-Helmholtz-related growth mechanisms, so we can exclude this mechanism in the present case except perhaps in the $r = 1/10$ case where a mode 2 is apparent in Fig. 18a.

The results are shown on Figs. 18 and 19 for several times and density ratios in a manner comparable to [2]. For these numerical experiments, the initialization of the velocity fields is rather important in order to not allow in the first time step some gas velocity in the liquid, and hence to avoid the situation of a boundary layer in the liquid in which the growth rate is independent of r as explained in Section 4.2.4. Thus the density is initialized to ρ_l to machine accuracy using the VOFI library [14,15] within a disk implicitly defined by $x^2 + y^2 < R^2$ and the *velocity* is initialized to 1 for all the velocity nodes inside a disk implicitly defined by $x^2 + y^2 < (R + nh)^2$, where n is the size of the "halo" in number of grid points. The velocity in the other nodes is initialized to 0. The tests shown were performed with $n = 1$. Increasing the size of the halo from $n = 1$ to $n = 2$ improves the results at early times ($\Delta t \leq D/U$) of the droplet motion, but not at late times ($\Delta t > D/U$).

The droplet momentum has been oriented along the diagonal as in [2]. The WY scheme is used with a QUICK-UW interpolant. The droplet deforms little after advection by one droplet diameter (Fig. 18). For longer advection the deformation is more pronounced but, as explained above, this is to be expected at high resolution, except in the $r = 10^{-9}$ case for which we show advection by 5 diameters in Fig. 19. If the non-consistent method is used, the droplet deforms rapidly and the simulation breaks down. Our results with the consistent method are better or on a par with previous results for early times ($\Delta t \leq D/U$) but for late times, $r = 10^{-9}$ and low order modes the results are somewhat worse than those of [2–5,7] (see Fig. 19). Finally for late times and more moderate density ratios it is difficult to asses the results because of the expected *physical* growth of perturbations as expressed for example in (63). As a comparison, in the results of the recent reference [7] there was no significant deformation after one "transit time"

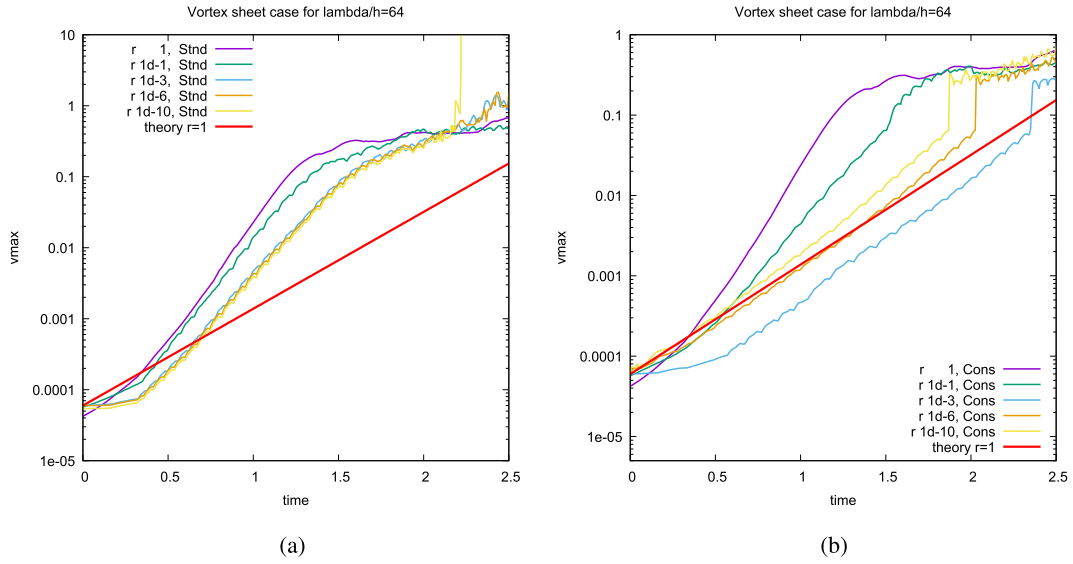

Fig. 16. Kelvin-Helmholtz instability in the vortex sheet case, with shift $\Delta z = h/2$, $\lambda/h = 64$ and different values of r. The theory for $r = 1$ is also plotted. (a) Non-consistent method. The growth rate is always much larger than in the theory, and it decreases with r, reaching a minimum around $r = 10^{-3}$. Around $t = 2.2$ the maximum of the velocity diverges for $r = 10^{-10}$. This divergence may be suppressed by using a smaller tolerance for the iterative Poisson solver for the pressure, but we keep it here for illustrative purposes. (b) Consistent method. The agreement between the $r = 10^{-6}$ case and the theory for $r = 1$ is coincidental. As the value of r is decreased, the growth rate first decreases, reaches a minimum around $r = 10^{-3}$ and then increases.

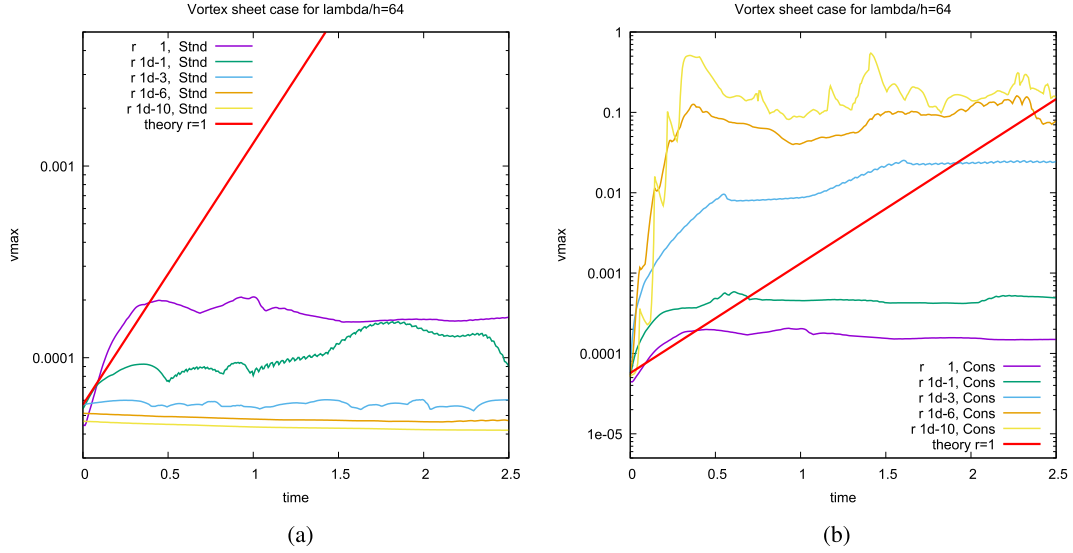

Fig. 17. Same parameters of Fig. 16 but with shift $\Delta z = 0$. (a) Standard method. At large r, the expected vanishing growth rate is achieved. (b) Consistent method. The amplitude of the maximum vertical velocity increases rapidly with increasing density contrast. For $r = 10^{-10}$ a super-fast increase is seen. This fast increase is made smaller when the clipping value ϵ_c is increased and is made even faster when ϵ_c is decreased.

$\Delta t = L_1/U_1$ which with the parameters of [7] corresponds to three diameters ($\Delta t = 3D/U$).

Further comments can be made on the causes of the droplet deformation, depending on whether the theoretical dynamics of the Kelvin-Helmholtz instability are correctly reproduced by the numerics or not. First, if the theory is approximately reproduced by the numerics, and the gas momentum numerically diffuses inside the liquid, then some vorticity may penetrate into the liquid despite the fact that in inviscid flow vorticity should remain confined on the interface. If this happens, then by the analysis of Section 4.2.4 the growth rate becomes independent of the density ratio r (Fig. 9), and has a much larger value of order $\omega_i \sim Uk$, without the $\sqrt{r}$ factor. Moreover, the instability seen for the $r = 10^{-9}$ case for the long advection case in Fig. 19 is a mode 3. If a low k mode such as mode 3 grows faster than the high frequency modes related to the grid, this indicates that a boundary layer has grown by numerical diffusion. The boundary layer is located at least in part in the liquid side otherwise it would have a much smaller growth proportional to $\sqrt{r}$.

Second, there could be an effect of the deviation from the Kelvin-Helmholtz theory. Indeed we observe spurious growth, especially at the end of Section 4.2.4. This could also be the cause of the deformation of the drop.

This points to two separate routes to the improvement of the results of this test: 1) by improving the method's performance for the vortex sheet case of the Kelvin-Helmholtz instability and minimising numerical diffusion; 2) by maximising numerical diffusion of vorticity into the gas phase and minimising diffusion of vorticity into the liquid phase. The first option would lead to a more accurate method, while the second one, even if successful for

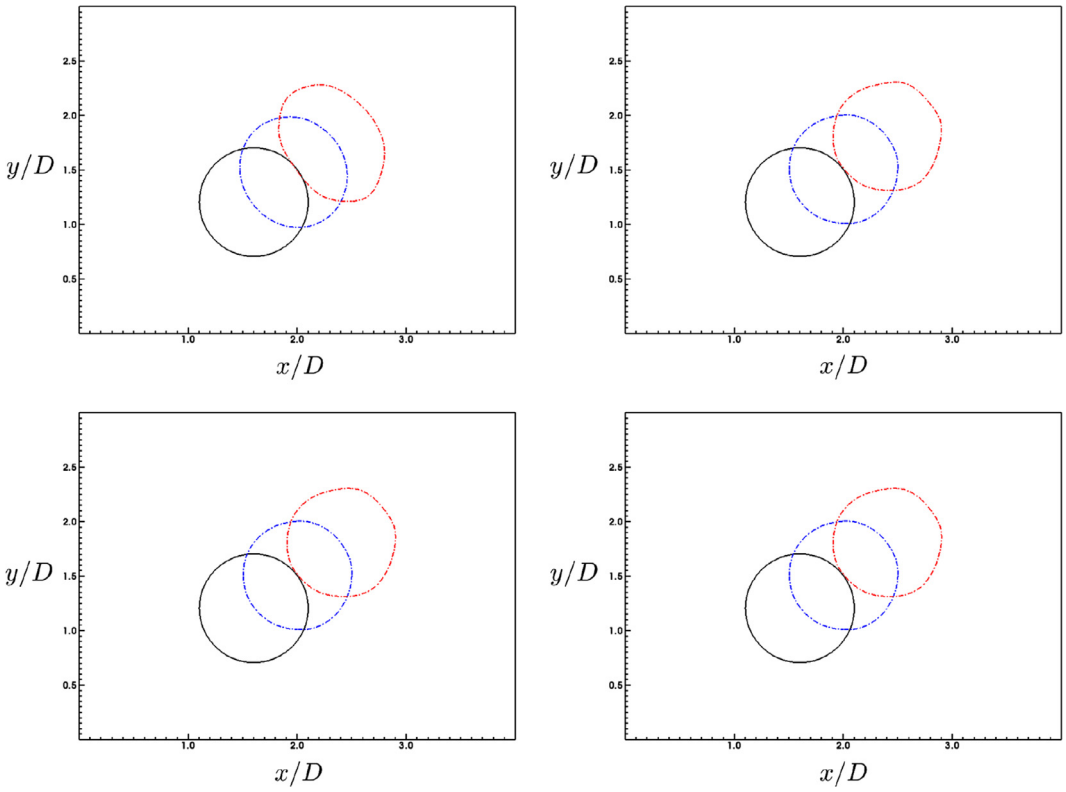

Fig. 18. Deformation of a droplet moving through a light fluid. The initial droplet resolution is $D/h = 20$. Black shape at $t = 0$, blue at $t = D/(2U)$ and red at $t = D/U$. Density ratios: $r = 10^{-1}, 10^{-3}, 10^{-6}, 10^{-9}$ (left to right and top to bottom). (For interpretation of the references to colour in this figure legend, the reader is referred to the web version of this article.)

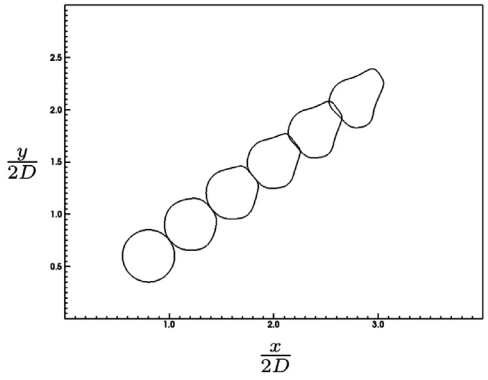

Fig. 19. Deformation of a droplet moving through a light fluid at $r = 10^{-9}$. The initial droplet resolution is $D/h = 20$.

the advected droplet test, would lead to an exceedingly diffusive code.

We note also that the tests of the Kelvin-Helmholtz instability in Section 4.2.4 are performed for interfaces aligned with the grid, while in this section interfaces may have any orientation with respect to the grid, so that even if vortex sheet dynamics were perfectly reproduced for interfaces aligned with the grid there would be no guarantee to have inviscid droplet dynamics represented correctly in all configurations and thus to have good results for the large density ratio droplet.

4.4. Sheared layer

In order to better analyze the behavior of the methods in flow under shear, such as vortex sheets and Kelvin Helmholtz instabilities, we set up a planar, parallel shear flow in a $(-1/2, 1/2)^2$ domain with the following initial conditions

$$u_1 = 15 \quad \text{if } |x_2| > 1/10$$
$$u_1 = 1 \quad \text{if } |x_2| < 1/10\,,$$

$$u_2 = 0.01\,\sin(2\pi x_1)\exp(-20x_2^2)\,,$$

$\rho = 1$ if $|x_2| > 1/10$, and $\rho = 10^3$ otherwise. This flow is similar to a liquid sheet in high velocity gas. The flow is simulated until time $t_f = 2$ unless the simulation blows up at an earlier time $t_b < t_f$. The crashes seem connected to the spurious growth of the Kelvin-Helmholtz instability described in Section 4.2.4. We note that the physical instability could lead to interface deformation, but not to the catastrophic increase of the total kinetic energy that is witnessed when the code crashes.

Table 1 shows the numerical schemes that have been used in a few simulations together with the fraction t_b/t_f of the final time that has been reached. All simulations have been performed on a 128×128 grid with a CFL of 0.03 and a density ratio of 1000. The consistent method is systematically more stable than the non-consistent one for the two combinations shown in

Table 1
Percentage of completion of the shear layer test with various methods. All simulations are performed on a 128×128 grid with a CFL of 0.03 and a density ratio of 1000.

Method	VOF Scheme	velocity scheme	fraction completed
non-consistent	WY	QUICK-UW	0.08
consistent	WY	QUICK-UW	0.17
non-consistent	CIAM	Superbee	0.50
consistent	CIAM	Superbee	1.

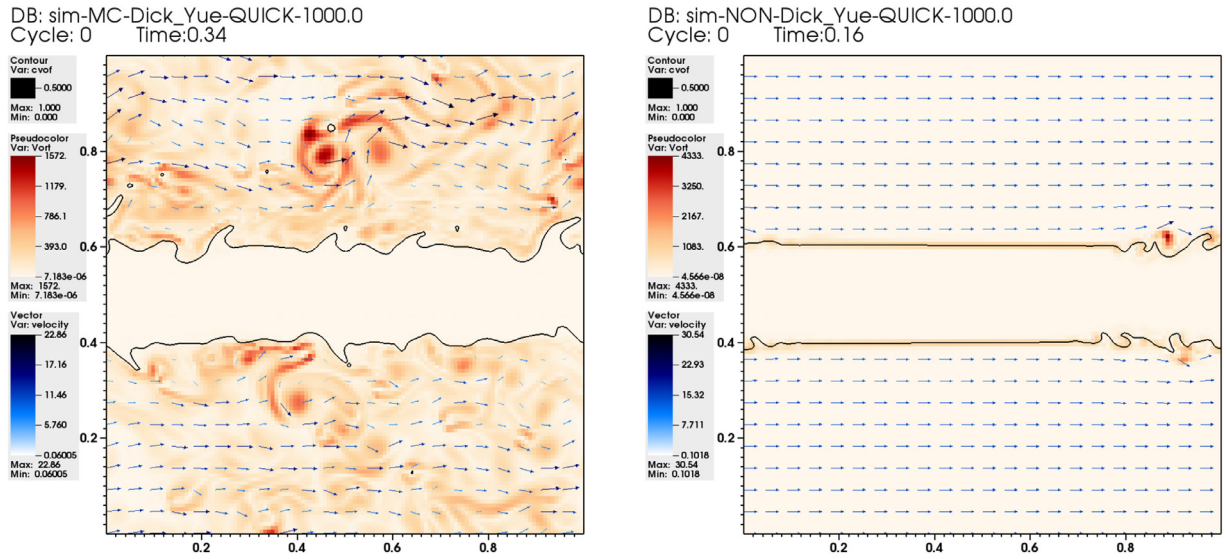

Fig. 20. The state of the simulation of the sheared layer just before its breakdown with the combination of WY VOF advection scheme and QUICK-UW velocity interpolation: consistent method (left), non-consistent method (right).

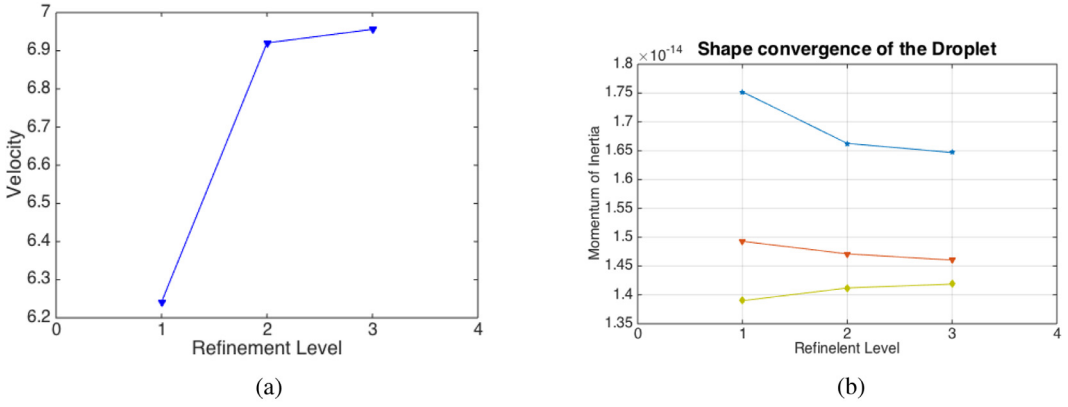

Fig. 21. Convergence of simulations. (a) Evolution of the terminal velocity with grid refinement. (b) Evolution of the three moments of inertia with grid refinement.

Table 1: a) the WY VOF scheme and the QUICK-UW velocity interpolation schemes and b) the CIAM VOF with the Superbee slope limiters. The state of the two simulations with the first combination of schemes is shown in Fig. 20, just before breakdown at time $t_b = 0.34$ (or $t_b/t_f = 0.17$) for the consistent method, and at time $t_b = 0.16$ (or $t_b/t_f = 0.08$) for the non-consistent method. We have also tested a number of other combinations, for example WY & Superbee that turns out to be very unstable. Furthermore, we have performed simulations with smaller 64×64 and 32×32 grids that yield similar results. Finally, we note that this case is also unstable in a single-phase configuration when using the QUICK third-order velocity interpolation.

4.5. Falling raindrop

A flow configuration that combines the complexities of large density contrasts with the interaction between capillary, viscous and inertial stresses is that of a water droplet falling in the air under the influence of gravity. From our experience it is this combination that leads to the blowups observed in many air-water simulations when a non-consistent method is used. We chose a falling water droplet in air of diameter $D = 3$mm, essentially a raindrop near the largest diameters (Fig. 22) for which sphericity is approximately maintained. This choice is motivated by the paradigmatic value of a near-spherical raindrop simulation, and by the fact that the corresponding Weber number (given below) is the same as in similar air-water suddenly-accelerated-droplet (or "secondary atomisation") simulations of [11,12]. We first define the problem in general terms and describe several variants of the simulation setup, then discuss the physics of droplet fall and the numerical results.

4.5.1. Problem setup

The droplet is placed at the center of a cubic domain of side L, with $L/D = 4$. The liquid properties ρ_l and μ_l correspond to water, and the gas properties ρ_g and μ_g correspond to air. We apply a uniform inflow velocity condition $u_1 = U_0(t)$ on the bottom face and an outflow velocity condition on the top face, corresponding to zero normal gradient. The droplet is subject to a gravity field g. Boundary conditions on the side walls are free-slip (no shear stress).

The subscripts l and g represent water and air phases respectively. The parameters in the problem setup are given in Table 2, and a schematic representation is given in Fig. 23. For $D = 3$mm experiments [33] indicate a terminal velocity close to $U_t = 8.06m/s$ which corresponds to a Weber number $\mathrm{We} = \rho_g U_t^2 D/\sigma \simeq 3.2$ similar to that tested by Xiao [11].

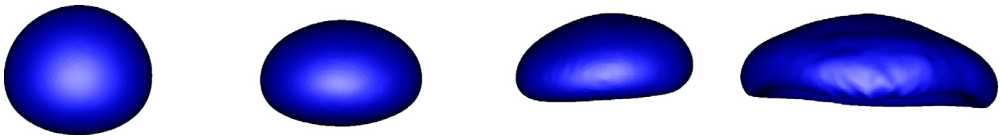

Fig. 22. Flattening of the droplet with increasing equivalent diameter. From left to right $D_e = 3$, 4.6, 6.4 and 8 mm.

Table 2
Parameter values used in the simulation of a falling water droplet in air.

ρ_g (kg/m^3)	ρ_l (kg/m^3)	μ_g $(Pa\,s)$	μ_l $(Pa\,s)$	σ (N/m)	D (m)	g (m/s^2)
1.2	0.9982×10^3	1.98×10^{-5}	8.9×10^{-4}	0.0728	3×10^{-3}	9.81

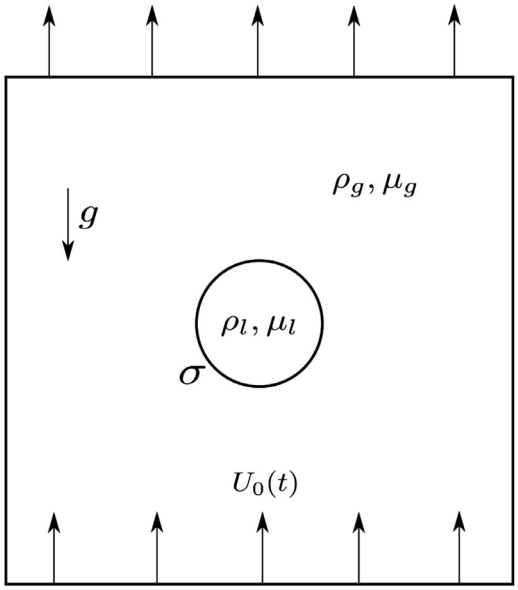

Fig. 23. The numerical setup for the falling raindrop. A droplet of diameter D is placed at the center of a cubic domain of side L, with $L/D = 4$. The liquid properties ρ_l and μ_l correspond to water, and the gas properties ρ_g and μ_g correspond to air. We apply a uniform inflow velocity condition $u_1 = U_0(t)$ on one face and an outflow velocity condition on the opposite face, corresponding to zero normal gradient. Boundary conditions on the side walls are free-slip (no shear stress).

We perform two main types of simulations

- Simulations in which the inflow velocity $U_0(t)$ is adjusted at each time step by a controller that aims at keeping the droplet at the center of the box.
- Simulations in which the inflow velocity has a constant value U_0.

The first type of simulations allows to keep the droplet near the center of the box for a long time without particular difficulties, but the controller adds some unwelcome jitters to the inflow velocity and as a result the frame of reference is not Galilean anymore, while the missing acceleration terms had not been added to the Navier–Stokes equations. Thus the simulations have only heuristic value. The second type has the droplet leaving the domain after a certain time, but is convenient for relatively short-time investigations. A third possible type of simulation, arguably the most natural one consists in using a much larger domain filled with air at rest, with zero inflow velocity and to let the droplet fall from the top of the domain. Note that Dodd and Ferrante [34] used such a setup. It is much more expensive and in fact smaller droplet diameters were investigated in [34].

In order to better grasp the physics of droplet fall, some understanding may be obtained from the fall of a solid object. Indeed, because of the large inertia of the liquid compared to the gas, during the first instants the droplet internal flow is comparatively negligible. Experiments and numerical simulations on falling solid spheres show that the drag coefficient is *larger* than the drag coefficient on a sphere held fixed, for example in a wind tunnel. At $\mathrm{Re} \simeq 10^3$ on finds $C_D \simeq 0.6$ to 0.7 for a falling sphere compared to $C_D \simeq 0.45$ for a fixed sphere (see for example [35] and references therein). (The difference between fixed and falling solids is probably due to the fluctuating center-of-mass velocity of the falling solids.) Drag coefficients $C_D \sim 0.6$–0.7 would result in a fall velocity of 6.8 to 7.3 m/s. The resulting difference between the falling velocity of water droplets and that of falling spheres may be explained as follows. The internal vortical motion probably results in a diminished friction between the droplet surface and the air flow and a resulting smaller drag coefficient, yielding the larger fall velocity. We detail the time scales related to the acceleration of the droplet and the internal motion below, and we perform numerical experiments in the two above setups. For the second setup we use two different inflow velocities.

4.5.2. Results with controlled inflow velocity

We use the controller setup with an initial inflow velocity $U_0(0) = 8$m/s. Three grids are used, with $D/h = 15, 30$ and 60. Numerical simulations of this test case at all resolutions carried out *without* the consistent scheme described in this paper result in the catastrophic deformations of the droplet that will be further investigated below. Using the consistent scheme, we avoid the instability and may observe the droplet for a long time with enough CPU resources (up to 200 ms for the $D/h = 32$ case) and may study the convergence of the terminal velocity and that of the shape. For the latter, we use as a descriptor of the shape the three moments of inertia I_{mm} defined by

$$I_{mm} = \int_{\mathcal{D}} H x_m^2 \mathrm{d}\mathbf{x}\,, \quad 1 \leq m \leq 3, \tag{64}$$

where $\mathcal{D}$ is the domain used for the computation and x_m is relative to the center of mass. The convergence of the moments of inertia and terminal velocity is shown on Fig. 21. The velocity seems to converge to a value around $7\,m/s$, which is consistent with the solid-sphere fall velocity.

4.5.3. Fixed 8m/s inflow velocity

We now use the fixed velocity setup with $U_0(t) = 8$m/s and perform simulations for very short times (of the order of 1 ms). Numerical simulations of this test case at moderate resolution (from $D/h = 16$ to $D/h = 64$) carried out *without* the consistent scheme described in this paper result in catastrophic deformations of the droplet illustrated in Fig. 24, a kind of 'fictitious' or 'artificial' atomization. These simulations display marked peaks or spikes in kinetic energy as a function of time, associated with massively-deformed interface shapes (see Fig. 28). Additionally, our studies suggest that certain combinations of the VOF advection method

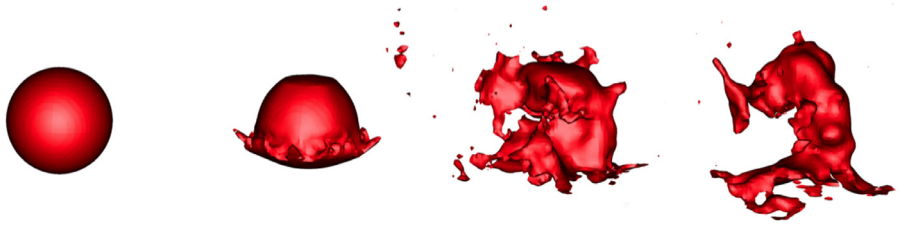

Fig. 24. Catastrophic deformation of a falling raindrop while using a version of our method that does not ensure consistency between mass and momentum transport ($D/h = 30$).

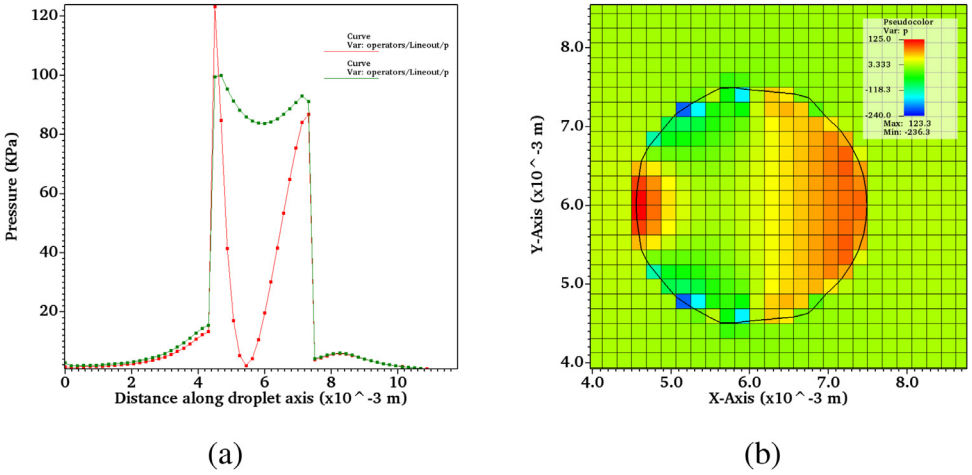

Fig. 25. The origin of the pressure peak in the front of the droplet. (a) Pressure profiles on the axis a few timesteps after initialization with the non-consistent method (red curve) and the consistent one (green curve). Much larger pressure gradients are present across the interface with the first method. (b) Pressure distribution immediately after the start of the simulation with the non-consistent method. The pressure peak has not yet resulted in the formation of a dimple. The initial droplet resolution is $D/h = 16$. The simulations are carried out with the CIAM advection method and the Superbee slope limiter. (For interpretation of the references to colour in this figure legend, the reader is referred to the web version of this article.)

and the velocity interpolation scheme are numerically more robust than others, in particular the most stable combinations are the CIAM advection with the Superbee slope limiter, and the WY advection with the QUICK-UW interpolation. This is in agreement with the results reported in Table 1.

We propose the following explanation in order to account for such numerical artifacts. To start with, we neglect gravity and viscous effects at this relatively large Reynolds number. Also, we are interested in steady-state flow. On the axis and near the hyperbolic stagnation point at the front of the droplet the tangential velocity is $u_2 = 0$ and the axial momentum balance is

$$u_1 \partial_1 u_1 = -\frac{1}{\rho} \partial_1 p. \tag{65}$$

Due to the large viscosity and density contrasts, it is not possible for the air flow to immediately entrain the water, so the fluid velocity is significantly smaller inside the droplet. In the air the acceleration near the stagnation point is of the order U^2/D, whereas the pressure gradient is

$$\partial_1 p \sim \rho_g U^2/D. \tag{66}$$

The pressure gradient in the water is much smaller, however, in the case of a mixed cell the water density multiplies the air acceleration U^2/D, so that

$$\partial_1 p \sim \rho_l U^2/D, \tag{67}$$

then a large pressure gradient results in the mixed cells. This large pressure gradient results in a large pressure inside the droplet near the front stagnation point, as shown in Fig. 25. This large pressure is balanced by surface tension only for a sufficiently large curvature near the droplet front. This explains the presence of a "dimple" often observed in low resolution simulations of the falling drop. This artifact has been observed by Xiao [11] in a similar case involving the sudden interaction of a droplet at rest with a uniform gas flow. The resulting large nonphysical pressure gradients across the interface eventually lead to its rapid destabilization and concomitant breakup.

Visualization of the flow around the droplet in Fig. 27 illustrates the challenging nature of the flow configuration, even for such a seemingly simple physical problem. As one can observe, the boundary layers are extremely thin. We observe that applying the numerical method described in this paper brings a considerable and systematic improvement over a spectrum of different velocity interpolation schemes and CFL numbers, as evidenced by comparing Figs. 25 and 26.

4.5.4. Convergence study at 5m/s inflow velocity

In this section we use the fixed inflow velocity setup but with smaller initial velocity. We systematically vary the resolution from $D/h = 8, 16, 32$ and 64. Despite using the consistent method, simulations at $D/h = 8$ are sometimes unstable, so we use a workaround and use a lower fixed inflow velocity of $U_0 = 5$ m/s, which differs from the expected long term terminal velocity $U_t \simeq 8$ m/s used in the previous section and also from the solid sphere terminal velocity. It however offers a milder initial condition and allows to observe the first phase of the (physical) acceleration towards the final statistical steady state. We perform simulations for $t_S = 5$ms (for reasons of CPU cost and because we do not want the droplet to get too close to the domain boundaries) and examine the convergence properties of the numerical system in this time frame.

In order to better understand the setup, it is useful to quickly review the relevant time scales.

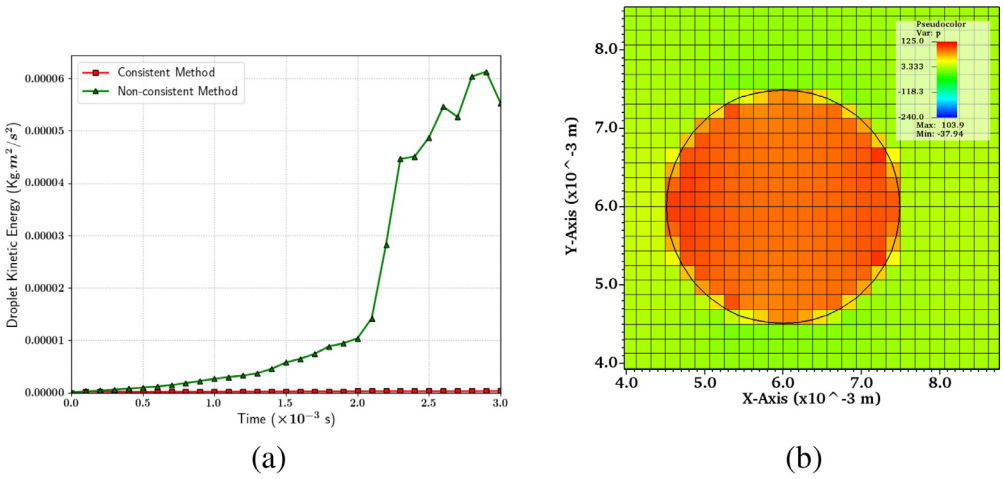

Fig. 26. (a) Comparison of the temporal evolution of droplet kinetic energy. The non-consistent method displays spikes in the kinetic energy that are 3 orders of magnitude larger than with the consistent method, leading to rapid destabilization. (b) Pressure distribution immediately after the start of the simulation with the consistent method. The initial droplet resolution is $D/h = 16$. The simulations are carried out with the CIAM advection method and the Superbee slope limiter.

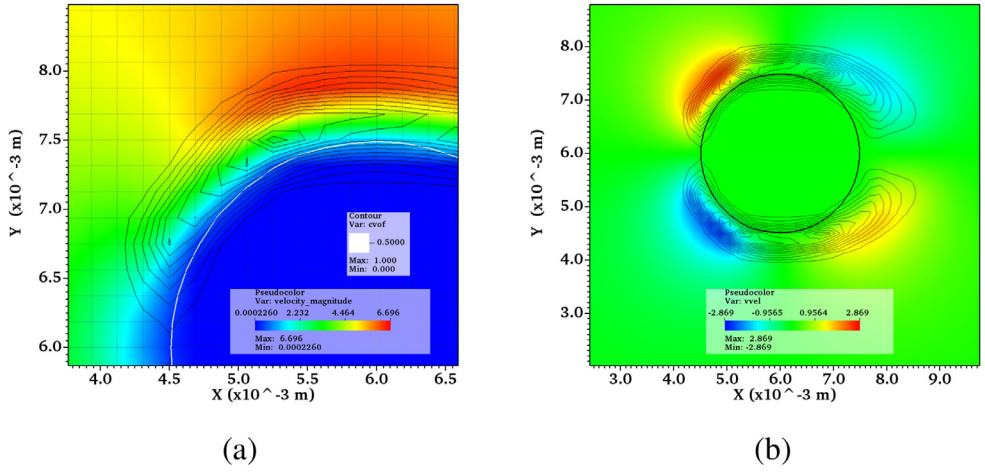

Fig. 27. Flow field around the 3 mm droplet immediately after the start of the simulation with the consistent method, demonstrating the contours of the magnitude of the vorticity field (black lines). The 2D cross-section in these two figures corresponds to the mid-plane slice along the z axis, with the inflow along the positive x axis and gravity opposite to it. (a) Velocity magnitude. The boundary layer is resolved by only 2–3 cells. (b) The velocity component in the y direction, perpendicular to the flow. As the flow develops further, a marked separation of the boundary layers is observed with a more complex vortical region in the wake. The initial droplet resolution is $D/h = 16$. The simulations are carried out with the CIAM advection method and the Superbee slope limiter.

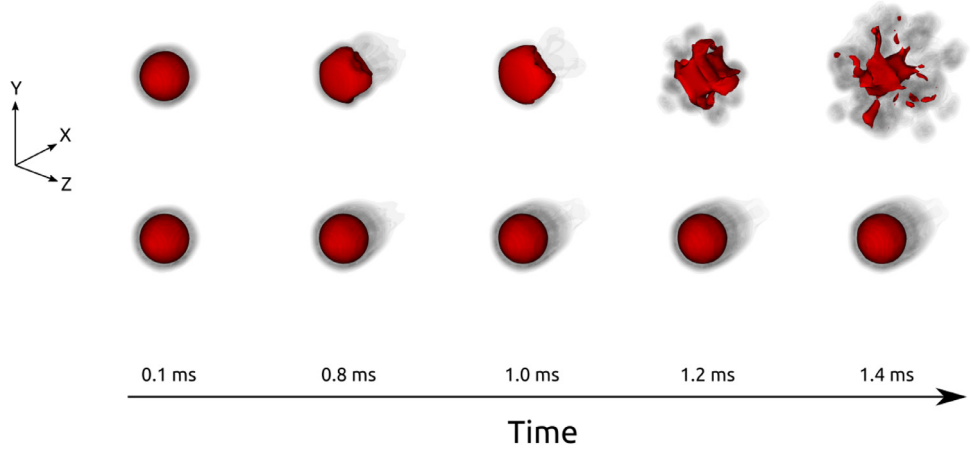

Fig. 28. A comparison of the temporal evolution between the non-consistent method (top row) and the consistent one (bottom row). The flow is along the positive x direction, with gravity opposite to it. The red contour indicates the isosurface of the volume fraction field corresponding to $C = 0.5$, whereas the black contours surrounding the drop represent isosurfaces of the magnitude of vorticity. The raindrop with the non-consistent method displays massive deformations leading to artificial breakup as a result of rapidly growing numerical instabilities. The initial droplet resolution is $D/h = 16$. The simulations are carried out with the CIAM advection method and the Superbee slope limiter. (For interpretation of the references to colour in this figure legend, the reader is referred to the web version of this article.)

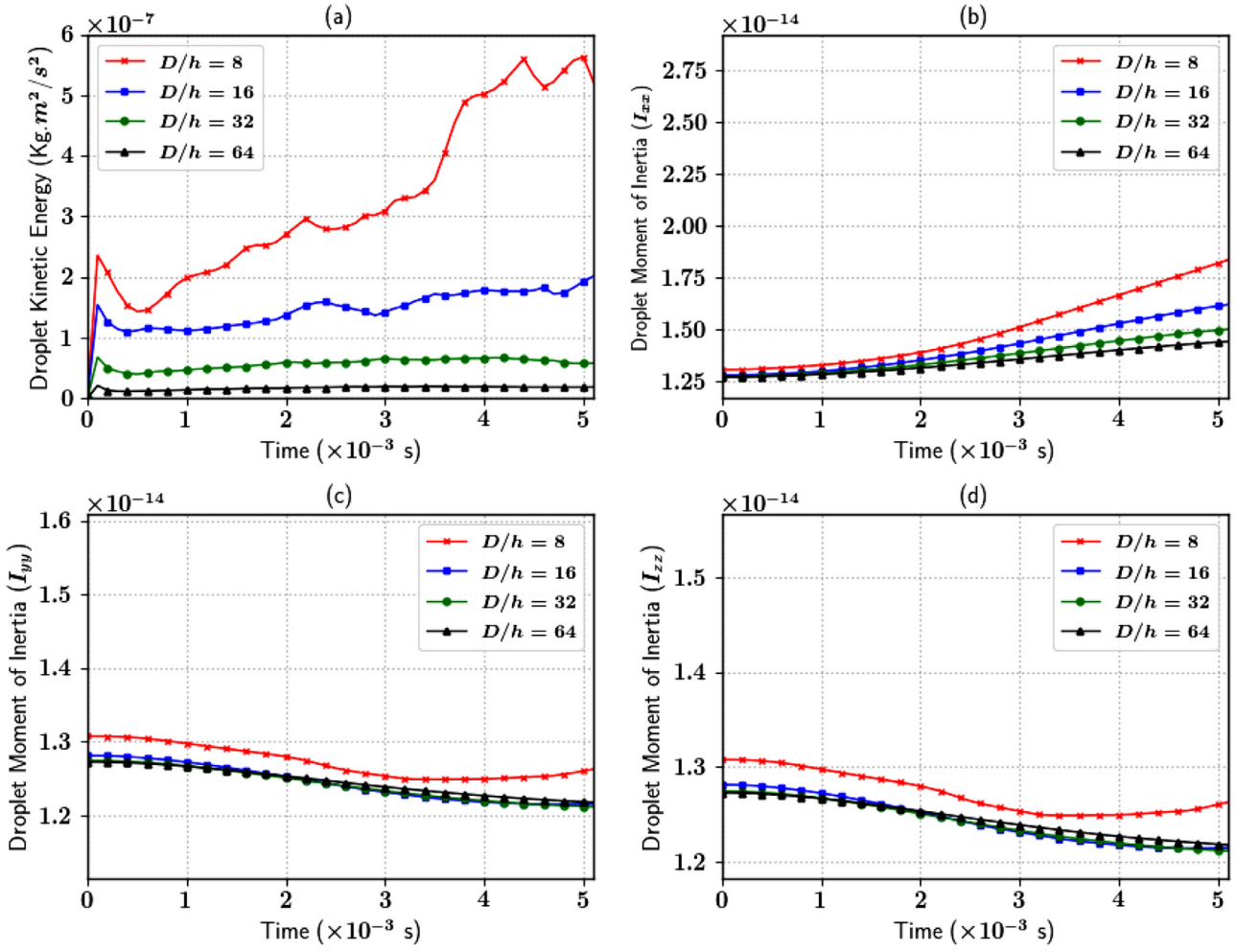

Fig. 29. Temporal evolution of a few physical quantities to evaluate the performance of our present method for different droplet resolutions D/h: (a) kinetic energy of the droplet; (b) moment of inertia I_{xx} of the droplet along the flow direction (x axis); (c) and (d) moments of inertia I_{yy} and I_{zz}.

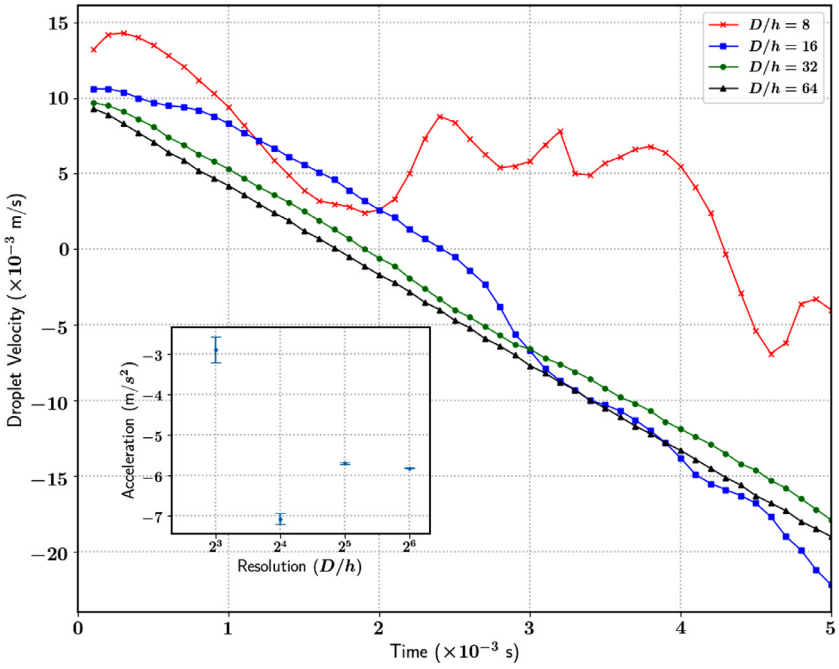

Fig. 30. Droplet velocity as a function of time, for different droplet resolutions D/h. The droplet velocity corresponds to that of the center of mass. Inset: convergence of the droplet acceleration as a function of its resolution, computed with the best linear fit over the temporal variation of the velocity. The error bar signifies the asymptotic standard error (least-squares) corresponding to the linear fit.

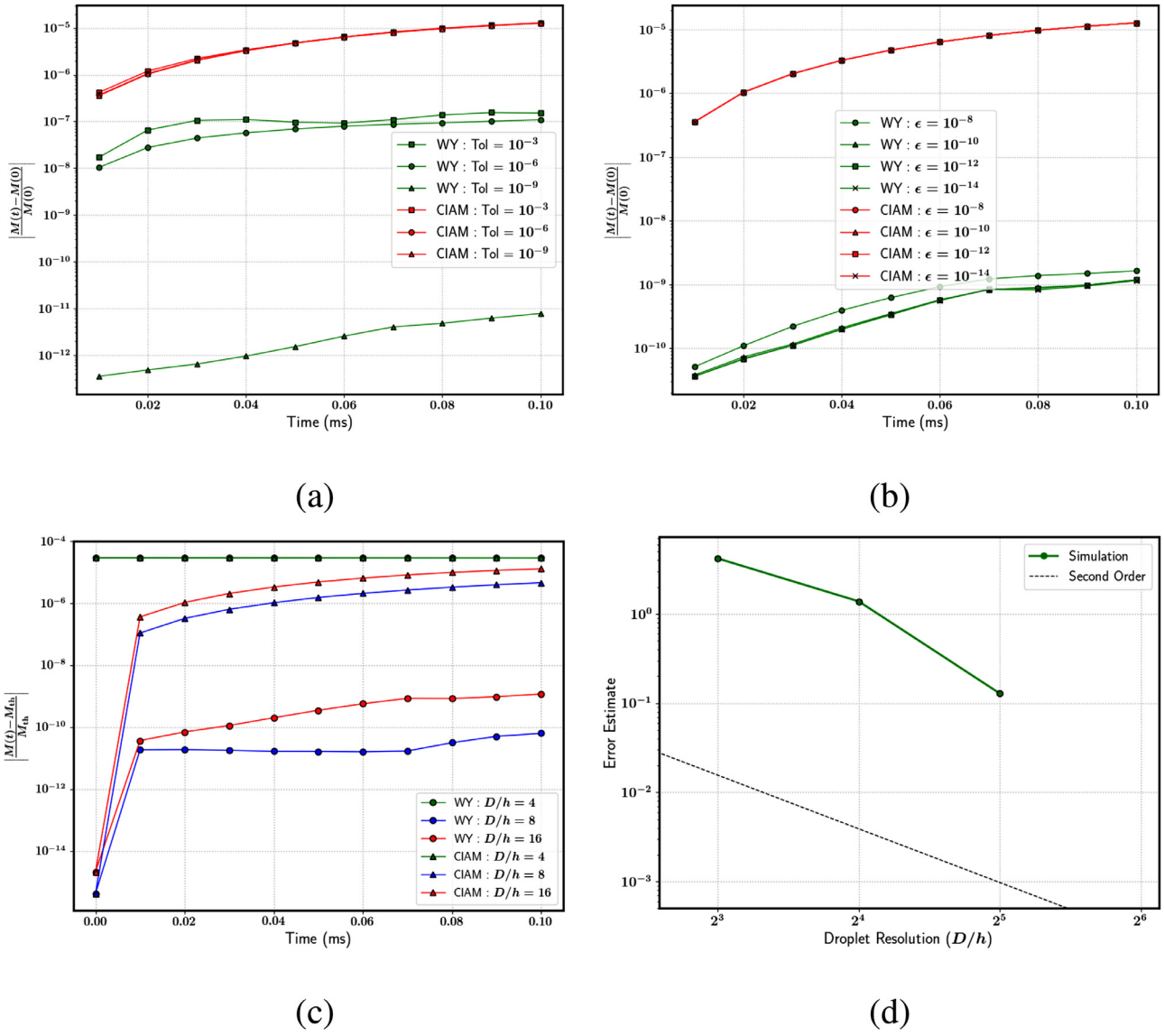

Fig. 31. Relative change in the droplet mass as a function of time in the first three plots. The simulations are carried out for a total time of 0.1 milliseconds, while the droplet resolution is $D/h = 16$ in the first two plots. The symbol "WY" in the legend refers to the combination of WY advection with the QUICK-UW velocity interpolation, and "CIAM" to the CIAM advection with the Superbee slope limiter. Mass conservation properties of the two schemes: (a) as a function of the Poisson solver tolerance; (b) as a function of the clipping parameter ϵ_c; (c) as a function of the droplet resolution D/h. (d) Error estimate on the droplet acceleration, in the frame of reference of the static box. The corresponding droplet accelerations are plotted in the inset of Fig. 30.

- The time scale $t_a = D/U_0$ of the air flow around the droplet, around 0.6 milliseconds, much shorter than the simulation time.
- The time $t_w = L/[2(U_t - U_0)] = 3$ ms that the droplet would take to travel by half the domain the domain once it had reached the terminal velocity. This time is not relevant here since one needs to wait first for the next two times before terminal velocity is reached.
- The time scale $t_c \simeq 15.1$ ms [36] of capillary oscillations of the droplet shape.
- The time scale t_i of relaxation to terminal velocity. Using the dynamics (68) below, this time is $\rho_l/\rho_g D/U_t = 215$ ms much longer than the simulation time.
- The time scale t_μ needed to entrain the internal vortical motion of the liquid under the action of the gas. An estimate this time is $D^2/\nu_l = \mathrm{Re}\, D/U_t = 400$ ms.

The time of relaxation may be estimated using a simple square-velocity drag law for the droplet. We model the droplet motion as a one-dimensional dynamics under the effect of gravity and drag as

$$\rho_l \frac{\pi D^3}{6}\frac{\mathrm{d}U}{\mathrm{d}t} = \rho_l \frac{\pi D^3}{6}\, g - C_D \rho_g \frac{\pi D^2}{8} U^2, \tag{68}$$

hence

$$\frac{\mathrm{d}U}{\mathrm{d}t} = -\frac{3}{4}\frac{r}{D}(U^2 - U_t^2) = -\frac{U - U_t}{t_i}, \tag{69}$$

where for $U \simeq U_t$

$$t_i = \frac{2}{3}\frac{D}{rU_t}, \tag{70}$$

which gives 205 ms.

It is interesting that the simulation time is inserted in the set of relevant time scales as $t_a \ll t_S \lesssim t_c \ll t_i < t_\mu$. This means we can see the effect of t_c in the data (especially the variation in time of the moments I_{mm}) but not the effect of the other time scales.

We use the WY advection scheme in combination with the QUICK-UW interpolation. The quantities of interest while examin-

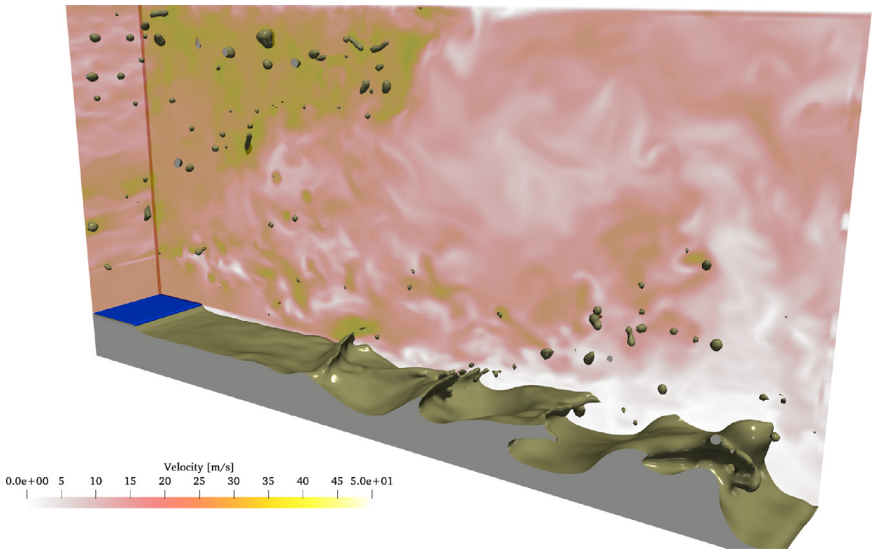

Fig. 32. Atomizing layer with air/water properties.

ing the robustness of the method are the temporal evolution of (Fig. 29a) and the moments of inertia (defined in Eq. 64) of the droplet along the three coordinate directions (Fig. 29b,c,d). These are used as a descriptor of the 'average' droplet shape. The droplet kinetic energy is defined relative to the droplet center-of-mass, that is

$$E_k = \langle \rho_l C(x,t) ||\mathbf{u}(x,t) - \mathbf{u}_{CM}(t)||^2 \rangle \tag{71}$$

where $\langle . \rangle$ is the spatial averaging operator of the entire domaine and $\mathbf{u}_{CM}(t)$ is the droplet center of mass. The kinetic energy of the droplet evolves in a relatively smooth manner, without the presence of sudden spikes and falls which are emblematic of the non-consistent version of our method (refer to Fig. 26). Such abrupt changes in kinetic energy of the droplet typically occur when the droplet undergoes 'artificial' atomization or breakup. We observe a strong decrease in the droplet kinetic energy as we increase resolution, an indication that low resolutions add considerable spurious jitter in the interfacial shape. Even at $D/h = 64$ the simulation is not converged in that respect. Finally, the moments of inertia of the droplet appear to evolve in a smooth manner for all droplet resolutions.

In Fig. 30, we show the velocity of the center of mass of the droplet (in the frame of reference of the box enclosing the droplet) as a function of time, and its behavior as we increase the droplet resolution. As one can observe it undergoes a near constant acceleration. The observed acceleration is $\frac{dU}{dt} \simeq 5.8 \pm 0.1$ m/s the error estimate being obtained from the difference between the 2^5 and the 2^6 values of the droplet resolution D/h. This is consistent with equation (69) if one sets $U = U_0$ and $U_t = 6.6$m/s not far from the terminal velocity of a solid sphere and of Section 4.5.2. One may also notice that on Fig. 30 the initial center-of-mass velocity is not zero in the simulation frame of reference but a small upward velocity of 10^{-2} m/s. This is due to the small velocity shift during the first time step projection already discussed in Section 4.3 of order $rU_0 \simeq 6\,10^{-3}$ m/s.

The temporal variation in the droplet velocity is fit to a straight line in order to evaluate the droplet acceleration for each droplet resolution. The estimated acceleration is shown in the inset of Fig. 30. The decrease of the error, obtained as above from the difference between successive resolutions is plotted on Fig. 31(d). No clear convergence order emerges, although the second-order convergence line is plotted to guide the eye.

In Fig. 31 we show the mass conservation properties of the two most stable combinations, that is the WY advection with the QUICK-UW velocity interpolation (WY) and the CIAM advection with the Superbee slope limiter (CIAM) for the falling raindrop. We have pointed out after (27) that the mass conservation of the WY advection is strongly dependent on how accurately the divergence-free condition is enforced, which in turns is determined by the Poisson's solver tolerance. A clipping procedure, with no redistribution, affects as well mass conservation. The WY combination is thus rather sensitive to these two parameters but overall performs much better than the CIAM combination which is inherently not mass-conserving (see (25)) and not very sensitive to the Poisson's solver tolerance and the parameter ϵ_c. Mass conservation is also plotted with various resolutions D/h in Fig. 31(c). It is seen that going from $D/h = 32$ to $D/h = 64$ the mass variation becomes larger for both methods, and grows over time at high resolution for WY, pointing to an accumulation of many machine precision errors.

4.6. Atomizing air and water planar jets

We also test the capability of the mass-momentum-consistent scheme to simulate an atomizing air-water shear flow. For that purpose we repeat the setup of ref. [37]. Two jets of air and water are entering the computational domain from the left of Fig. 32 at velocities comparable to those of experiments. However in order to save computer time the computational domain is smaller than the experimental one. Physical properties of air and water are identical to those of the falling raindrop case given in Table 2. The flow and domain characteristics are given in Table 3 including a gas boundary layer and separator-plate identical to those of ref. [37]. The notations are as in ref. [37]: H_p is the thickness of the jet of phase p, there is a separator plate of thickness l_y and a gas boundary layer of thickness δ_g. The two streams have equal thickness $H_l = H_g$. The dimensionless parameters are given in Table 4. The CIAM advection method has been used. The number of grid points in the layer

Table 3
Physical parameters (defined in the text) for the atomizing layer setup. The fluid properties are the same as in Table 2.

U_l (m/s)	U_g (m/s)	H_l (m)	h (m)	l_y (m)	δ_g/l_y $(-)$
1	25	$4\,10^{-3}$	$2.5\,10^{-4}$	$2.5\,10^{-4}$	2

Table 4
Dimensionless parameters for the atomizing layer setup.

M $\rho_g U_g^2/(\rho_l U_l^2)$	r ρ_l/ρ_g	m μ_l/μ_g	$\mathrm{Re}_{g,\delta}$ $\rho_g U_g H_g/\mu_g$	$\mathrm{We}_{g,\delta}$ $\rho_l U_l H_l/\mu_l$	Re_g $\rho_g U_g^2 H_g/\sigma$
0.75	831.8	45	757.6	5.151	6061

$H_l/h = 16$ is relatively small, when compared to $H_l/h = 32$ in the coarsest simulation of ref. [37]. It is thus all the more remarkable that the simulation is stable since using a smaller number of grid points usually increases the trend towards instability. It is interesting to note that the VOF calculations accounts for 31.5% of the total time, while the inversion of the Poisson operator for the pressure accounted for 51.5%. The whole simulation runs overnight on a present-day workstation.

5. Conclusion

We have presented and tested a new simulation method for multiphase flow that involves momentum advection that is consistent with VOF advection. The method includes an implementation of the WY VOF advection method.

A simple and fast test of the method's stability and accuracy is offered by the analysis of the Kelvin-Helmholtz instability. The method is converging when velocity profiles are continuous. However in the case of vortex sheets spurious growth is often observed. Progress on this front would probably provide benefits on other aspects of the method's performance.

The increased stability of the new method, on the other hand is evidenced in several classical tests cases and especially for a 3 mm droplet of water falling in air, a typical raindrop. It is a reflection on the challenging nature of multiphase flow that such complex methods apparently need to be implemented to resolve such an everyday and simple phenomenon.

The method comes with a significant saving of computer time, since for similar problems with raindrops, our attempts with a non-momentum-consistent VOF approach led to catastrophic deformation of the drop or strong dimple formation. These problems have also been observed by us using other non-VOF-consistent and non-momentum-consistent methods such as the one of [24]. In that case whenever less than 200 grid points per diameter are used numerically stable air-water drops accelerated at moderate Weber number cannot be found. However for higher resolutions they can be computed without difficulty as also found by the authors of ref[38]. Here, approximate solutions for the raindrop accurate within 15% are found with only 15 points per diameter. At lower resolution, down to 2 points per diameter the simulations are often stable, but the new method is unable to stabilize them in all conditions.

A particular advantage of the method is that it is conserving mass at the accuracy at which discrete incompressibility is enforced and opens a perspective for similar momentum conservation using WY advection. The method nevertheless is more complex and costly than a collocated method. This opens the perspective for systematic development of other methods with different grid arrangements. Another perspective is the potential of stable methods with large density contrasts, exact mass and momentum conservation and small droplets, that could be smoothly merged into models that represent the small droplets as Lagrangian Point Particles [39].

Credit Author Statement

Among the authors, Gretar Tryggvason, Ruben Scardovelli, Yue Ling and Stphane Zaleski have been involved in the construction of the base of the ParisSimulator VOF and Front- Tracking code that was used to implement and test the ideas in this paper. Daniel Fuster was involved in the development of the momentum advection method consistent with VOF advection, with help from Tomas Arrufat, Leon Malan and Yue Ling. The Kelvin-Helmholtz analysis and testing were done by Stphane Zaleski. The falling raindrop testing and the corresponding figures were done by Tomas Arrufat for the controlled inflow velocity part 4.5.2 and Sagar Pal for the fixed inflow velocity parts 4.5.3 and 4.5.4. The large density droplet and shear layer tests were done by Sagar Pal. The testing for a droplet suddenly accelerated in a carrying gas at rest and for a sheared layers were done by Sagar Pal. The atomisation testing was done by Marco Crialesi-Esposito.

Declaration of Competing Interest

The authors declare that they have no known competing financial interests or personal relationships that could have appeared to influence the work reported in this paper.

Acknowledgements

This work has been supported by the ANR MODEMI project (ANR-11-MONU-0011) program, grant SU-17-R-PER-26-MULTIBRANCH from Sorbonne Université and the ERC Advanced Grant TRUFLOW.

This work was granted access to the HPC resources of TGCC-CURIE, TGCC-IRENE and CINES-Occigen under the allocations t20152b7325, t20162b7760, 2017tgcc0080 and A0032B07760, made by GENCI and TGCC. The authors would also like to acknowledge the MESU computing facilities of Sorbonne Université.

We would like to thank Dr. W. Aniszewski, Dr. S. Dabiri, Dr. Jiacai Lu and Dr. Ph. Yecko for their contribution to the development of the code *PARIS-Simulator*, and we thank Dr. W. Aniszewski, Dr. V. Le Chenadec, Dr. C. Pairetti, Dr. S. Popinet and Dr. S. Vincent for useful conversations on the topics of this paper.

Finally, the simulation data are visualized by the software VisIt developed by the Lawrence Livermore National Laboratory.

Appendix A. Interpolations for the advected velocity component $\phi = \tilde{u}_q$

We want interpolate the value of ϕ on the face between the two centered values $\phi_{-1/2}$ and $\phi_{1/2}$ of Fig. 4, where we have already interpolated with a centered scheme the advecting velocity u_f perpendicular to the face. We consider the interpolating function (59)

$$\phi_0 = f\left(\phi_{-3/2}, \phi_{-1/2}, \phi_{1/2}, \phi_{3/2}, \mathrm{sign}(u_f)\right).$$

In the first scheme we use QUICK, a third order interpolant, away from the interface and a first-order upwind scheme near the interface. For positive advecting velocity, $u_f > 0$, and in the bulk we have

$$\phi_0 = \frac{3}{4}\phi_{-1/2} + \frac{3}{8}\phi_{1/2} - \frac{1}{8}\phi_{-3/2}, \tag{A.1}$$

while near the interface the upwind value is $\phi_0 = \phi_{-1/2}$. For negative advecting velocity, $u_f < 0$, and in the bulk we have

$$\phi_0 = \frac{3}{4}\phi_{1/2} + \frac{3}{8}\phi_{-1/2} - \frac{1}{8}\phi_{3/2}, \tag{A.2}$$

while near the interface $\phi_0 = \phi_{1/2}$.

In the second scheme we use a Superbee slope limiter away from the interface. For a positive advecting velocity u_f, we consider the general family of interpolants

$$f(\phi_{-3/2}, \phi_{-1/2}, \phi_{1/2}, \phi_{3/2}, \mathrm{sign}(u_f)) = \phi_{-1/2} + Sh/2, \tag{A.3}$$

where the slope S is given by a slope-limiter function g, $S = g(\phi_{-3/2}, \phi_{-1/2}, \phi_{1/2})$. For a negative advecting velocity $u_f < 0$ we consider

$$f(\phi_{-3/2}, \phi_{-1/2}, \phi_{1/2}, \phi_{3/2}, \text{sign}(u_f)) = \phi_{1/2} - Sh/2\,, \tag{A.4}$$

where $S = g(\phi_{-1/2}, \phi_{1/2}, \phi_{3/2})$. For $u_f > 0$, the two slopes

$$\alpha^+ = \left(\phi_{1/2,j} - \phi_{-1/2,j}\right)/h\,, \qquad \alpha^- = 2\left(\phi_{-1/2,j} - \phi_{-3/2,j}\right)/h\,, \tag{A.5}$$

are first estimated, to compute

$$\alpha = \min\left(\alpha^+, \alpha^-\right), \tag{A.6}$$

then the other two slopes

$$\beta^+ = 2\left(\phi_{1/2,j} - \phi_{-1/2,j}\right)/h\,, \qquad \beta^- = \left(\phi_{-1/2,j} - \phi_{-3/2,j}\right)/h\,, \tag{A.7}$$

to compute

$$\beta = \min\left(\beta^+, \beta^-\right), \tag{A.8}$$

Finally the slope S is given by the expression

$$S = \max\left(0, \alpha, \beta\right). \tag{A.9}$$

A similar development can be done for $u_f < 0$.

A slightly different estimate of the Superbee advected velocity is used near the interface. First we extend the definition of the interpolants as we shall predict $\bar{u}_q$ at a point $\hat{x}$ slightly upwind from x_f using a new function $\hat{f}$ so that

$$\phi_0 = \hat{f}\left(\hat{x}, \phi_{-3/2}, \phi_{-1/2}, \phi_{1/2}, \phi_{3/2}, \text{sign}(u_f)\right). \tag{A.10}$$

We take $\hat{x} = x_f - u_f\tau/2$ to be the midpoint of the fluxed region Ω_D of Fig. 4(b). The extended interpolant is defined for positive velocity u_f as

$$\hat{f}\left(\hat{x}, \phi_{-3/2}, \phi_{-1/2}, \phi_{1/2}, \phi_{3/2}, \text{sign}(u_f)\right) = \phi_{-1/2} + S|\hat{x} - x_{-1/2}| \tag{A.11}$$

and for negative velocity u_f as

$$\hat{f}\left(\hat{x}, \phi_{-3/2}, \phi_{-1/2}, \phi_{1/2}, \phi_{3/2}, \text{sign}(u_f)\right) = \phi_{1/2} - S|\hat{x} - x_{1/2}| \tag{A.12}$$

The rationale behind this choice is as follows. For a time-independent advecting velocity field $u(\mathbf{x})$, the integrals in expression (44) can be simplified

$$\phi_0 = \bar{u}_q = \frac{\int_{\Omega_D} u_f u_q \,\mathrm{d}\mathbf{x}}{\int_{\Omega_D} u_f \,\mathrm{d}\mathbf{x}}. \tag{A.13}$$

where Ω_D is the "donating region" of Fig. 4(b). We approximate the advecting velocity u_f by its midpoint value and the integral can be further simplified as

$$\bar{u}_q = \frac{1}{|\Omega_D|}\int_{\Omega_D} u_q \,\mathrm{d}\mathbf{x} \tag{A.14}$$

Since the "midpoint" at $\hat{x}$ is the center of mass of the donating region Ω_D the interpolation expression (A.10) follows.

Appendix B. Kelvin Helmholtz instability: numerical setup

We consider the 2D base flow shown on Fig. 8. Coordinates are noted (x, z) and vectors (u, w). The height of the interface is $h(x, t)$. The flow has density ρ_1 for $z < h(x, t)$ and ρ_2 for $z > h(x, t)$ and is incompressible. The base flow is a parallel shear flow. The base flow is uniform with $u = -U$ for $z < 0$ and $u = U$ for $z > 2a$, with a linear (Couette flow) boundary layer in between. When $\rho_1 \neq \rho_2$ the heavier fluid is the "liquid" and the lighter the "gas". For $\rho_1 > \rho_2$ the boundary layer is in the gas while otherwise the bounary layer is in the liquid. Similar flows have been studied in [40,41].

B1. Dispersion relation

The Euler and incompressibility equations are as in Eqs. (4) with only $\mathcal{L} = \mathcal{L}_{\text{conv}}$, surface tension and viscosity are not included. The interface height h moves according to

$$\partial_t h + u\partial_x h = w \tag{B.1}$$

We also use a stream function ψ

$$w = -\partial_x \psi\,, \quad u = \partial_z \psi \tag{B.2}$$

We consider a small perturbation of the base velocity in the form

$$\mathbf{u} = \mathbf{u}_0 + \epsilon\mathbf{u}_1 + \mathcal{O}(\epsilon^2) \tag{B.3}$$

the pressure expands as $p = p_0 + \epsilon p_1(x, z, t) + \mathcal{O}(\epsilon^2)$, the height as $h = \epsilon h_1(x, z, t) + \mathcal{O}(\epsilon^2)$, and similarly the stream function. We assume the following form for the perturbation

$$\begin{pmatrix} u_1 \\ w_1 \\ p_1 \\ \psi_1 \\ h_1 \end{pmatrix} = \begin{pmatrix} U_1(z) \\ W_1(z) \\ P_1(z) \\ \Psi_1(z) \\ A_h \end{pmatrix} e^{-\mathrm{i}kx - \mathrm{i}\omega t} \tag{B.4}$$

where k is an arbitrary wavenumber and ω a frequency to be determined. Although the expressions on the rhs in (B.4) are complex we understand the real part.

It is convenient to define as Chandrasekhar [42] the reduced wavenumber $\kappa = 2ka$ and the reduced frequency $\Omega = \omega a/U$, which are related by

$$e^{-2\kappa} = (1 - 2\Omega - \kappa)\frac{2 + (r+1)(2\Omega - \kappa)}{2 + (r-1)(2\Omega - \kappa)}, \tag{B.5}$$

see for example [41], equation (135). The system is unstable whenever Eq. (B.5) has two complex conjugate non-real roots. Then the positive imaginary part Ω_i is the growth rate, plotted on Fig. 9 in the cases $r = 1, 10$ and 100 where $r = \max(\rho_1/\rho_2, \rho_2/\rho_1)$. The case $\rho_1/\rho_2 = 100$ corresponds to the boundary layer in the gas and is much less unstable than the case with the boundary layer in the liquid. As the ratio $\rho_1/\rho_2 = 100$ is increased the growth rate for the boundary layer in the gas decreases steadily while the growh rate for the boundary layer in the liquid converges to the one for a free surface, with the gas replaced by a void.

B2. Special case

When $a = 0$ the above is singular and a special computation, performed in Section B.5 below, is needed. One has $\kappa = 0$ and the frequencies are

$$\omega = \left(\frac{r-1}{r+1} + \frac{2\sqrt{r}}{r+1}\mathrm{i}\right)kU \tag{B.6}$$

B3. Construction of the unstable mode

We want to write the solution using the stream function ψ in order to have a divergence free initial condition in the computations. We introduce four arbitrary constants noted A_0 and B_0 in the region $0 < z < 2a$, A_1 in the region $z < 0$ and B_2 in the region $z > 2a$, so that ψ is given by

$$z < 0 \psi(x, z, t) = A_1 e^{kz} e^{-\mathrm{i}kx - \mathrm{i}\omega t} \tag{B.7}$$

$$0 < z < 2a \psi(x, z, t) = (A_0 e^{kz} + B_0 e^{-kz}) e^{-\mathrm{i}kx - \mathrm{i}\omega t} \tag{B.8}$$

$$2a < z \psi(x, z, t) = B_2 e^{-kz} e^{-\mathrm{i}kx - \mathrm{i}\omega t} \tag{B.9}$$

We also introduce four additional constants noted A'_0 and B'_0 in the region $0 < z < 2a$, A'_1 in the region $z < 0$ and B'_2 in the region $z > 2a$.

$$z < 0 W_1(z) = A'_1 e^{kz} \tag{B.10}$$

$$0 < z < 2a W_1(z) = A'_0 e^{kz} + B'_0 e^{-kz} \tag{B.11}$$

$$2a < z W_1(z) = B'_2 e^{-kz} \tag{B.12}$$

After substitution in the Euler equations one obtains the pressure perturbation in the three regions; for $z < 0$,

$$P_1(z) = \frac{\mathrm{i}\rho_1}{k}(\omega - kU)(A'_0 + B'_0)e^{kz}, \tag{B.13}$$

for $0 < z < 2a$,

$$P_1(z) = \frac{\mathrm{i}\rho_2}{k}\left[(\omega + kU\frac{z}{a} - kU)(A'_0 e^{kz} - B'_0 e^{-kz}) - (A'_0 e^{kz} + B'_0 e^{-kz})\frac{U}{a}\right] \tag{B.14}$$

and for $z > 2a$,

$$P_1(z) = -\frac{\mathrm{i}\rho_2}{k}(\omega + kU)(B'_0 + A'_0 e^{4ka})e^{-kz}. \tag{B.15}$$

From (B.1)

$$\partial_t h = -U_0(0)\partial_x h + w \tag{B.16}$$

and from (B.2) and (B.8) we get

$$-\mathrm{i}\omega A_h = -\mathrm{i}kUA_h + \mathrm{i}k(A_0 + B_0)$$

hence

$$(-\mathrm{i}\omega + \mathrm{i}kU)A_h = \mathrm{i}k(A_0 + B_0)$$

and

$$A_h = -\frac{k}{\omega - kU}(A_0 + B_0)$$

Similar relations are obtained from the requirements of continuity of pressure and normal velocity at $z = 0$ and $z = 2a$. We can then determine all the amplitudes of the constructed solution after an amplitude for the interface has been chosen. Typically the modulus $|A_h|$ and the argument ϕ are selected so that

$$A_h = |A_h|e^{\mathrm{i}\phi}$$

then for $\kappa > 0$ we have

$$C_0 = -(\frac{\omega}{k} - U)A_h(e^{-2\kappa} + 2\Omega + \kappa - 1)^{-1} \tag{B.17}$$

$$A_0 = C_0 e^{-2\kappa} \tag{B.18}$$

$$B_0 = C_0(2\Omega + \kappa - 1) \tag{B.19}$$

$$A_1 = A_0 + B_0 \tag{B.20}$$

$$B_2 = A_0 e^{2\kappa} + B_0 \tag{B.21}$$

These expressions for the amplitudes together with (B.7–B.9) are used to initialize the stream function. The intermediate constant C_0 is used to simplify the expressions.

B4. Special cases: mode structure for $ka \to 0$

B4.1. Mode structure for $a > 0$ going to the limit $a \to 0$.

For small or vanishing a and κ however the expression (B.17) is singular. Indeed in the limit $\kappa \to 0$ we also have $\Omega \to 0$ and

$$e^{-2\kappa} + 2\Omega + \kappa - 1 = -2\kappa + 2\kappa^2 + \kappa + \mathcal{O}(\kappa^3) = -\kappa + \mathcal{O}(\kappa^2)$$

and then A_0 and B_0 become spurious as the region $(0, 2a)$ vanishes. From (B.17)

$$C_0 \simeq -\frac{\omega}{k}\frac{1}{\kappa}A_h$$

and from (B.19) and (B.21)

$$B_2 = C_0(2\Omega + \kappa) \simeq \kappa C_0$$

Thus for $a = 0$

$$B_2 = -\frac{\omega}{k}A_h$$

$$A_1 = \frac{\omega}{k}A_h$$

the latter being obtained directly from (B.20). Since $B_2 \neq A_1$ there is a $\mathcal{O}(\epsilon)$ discontinuity of ψ which results in a jump of $v(x, z, t)$ accross the interface at $z = 0$ and a related thin jet $u_1(x, z, t) \simeq \epsilon f(x, t)\delta(z)$. This is a consequence of placing the interface in the above calculations at $z = 0$ instead of $z = \epsilon h_1(x, t)$ and it conflicts with the solution obtained classically and also below with the thin vortex sheet setup (that is, the setup in which $a = 0$ is postulated at the beginning).

B5. Mode structure in the $a = 0$ case

We now obtain the mode structure for the classic thin vortex sheet setup where one assumes $a = 0$ from the start. In that case we keep only the terms in (B.7) and (B.9). The velocity continuity condition becomes

$$h_t = -uh_x + w = -u_0 h_x + w_1 + \mathcal{O}(\epsilon) \tag{B.22}$$

which replaces (B.16). Since h_t must have the same expression above and below the interface

$$[w - h_x u_0] = 0 \tag{B.23}$$

thus $[w] = h_x[u_0] = 2h_x U$ and from (B.10) and (B.12)

$$z < 0 W_1 = A'_1 e^{kz} \tag{B.24}$$

$$z > 0 W_1 = B'_2 e^{-kz} \tag{B.25}$$

and from (B.22)

$$A'_1 = -\mathrm{i}(\omega - kU)A_h \tag{B.26}$$

$$B'_2 = -\mathrm{i}(\omega + kU)A_h \tag{B.27}$$

The pressure equality at $z = 0$ leads to

$$z < 0 P_1 = \frac{\mathrm{i}\rho_1}{k^2}(\omega - kU)A'_1 k e^{kz} \tag{B.28}$$

$$z > 0 P_1 = \frac{\mathrm{i}\rho_2}{k^2}(\omega + kU)B'_2(-k e^{-kz}) \tag{B.29}$$

hence introducing $\nu = \omega/(kU)$ and from (B.26) and (B.27)

$$(\nu + 1)A_1 - (\nu - 1)B_2 = 0 \tag{B.30}$$

$$r(\nu - 1)A_1 + (\nu + 1)B_2 = 0 \tag{B.31}$$

from which one obtains

$$\nu = \frac{r-1}{r+1} + \frac{2\sqrt{r}}{r+1}\mathrm{i} \tag{B.32}$$

identical to (B.6). Also from (B.26) and (B.27)

$$A_1 = (U - \omega/k)A_h \tag{B.33}$$

$$B_2 = -(U + \omega/k)A_h. \tag{B.34}$$

These expressions should be used whenever $a \ll A_h$ while the full expressions with the boundary layer would be valid for $A_h \ll a$. In both cases $\Delta x \ll \min(A_h, a)$ ma be required.

References

[1] Rudman M. A volume-tracking method for incompressible multi-fluid flows with large density variations. Int J Numer Meth Fluids 1998;28:357–78.
[2] Bussmann M, Kothe DB, Sicilian JM. Modeling high density ratio incompressible interfacial flows. In: ASME 2002 joint US-European fluids engineering division conference. American Society of Mechanical Engineers; 2002. p. 707–13.
[3] Desjardins O, Moureau V. Methods for multiphase flows with high density ratio. Center for Turbulent Research, Summer Programm 2010;2010:313–22.
[4] Raessi M, Pitsch H. Consistent mass and momentum transport for simulating incompressible interfacial flows with large density ratios using the level set method. Computers & Fluids 2012;63:70–81.
[5] Le Chenadec V, Pitsch H. A monotonicity preserving conservative sharp interface flow solver for high density ratio two-phase flows. J Comput Phys 2013;249:185–203.
[6] Vaudor G, Menard T, Aniszewski W, Doring M, Berlemont A. A consistent mass and momentum flux computation method for two phase flows. application to atomization process. Computers & Fluids 2017;152:204–16.
[7] Zuzio D, Orazzo A, Estivalèzes J-L, Lagrange I. A new efficient momentum preserving level-set/vof method for high density and momentum ratio incompressible two-phase flows. J Comput Phys 2020;410:109342.
[8] Saurel R, Abgrall R. A multiphase Godunov method for compressible multifluid and multiphase flows. J Comput Phys 1999;150(2):425–67.
[9] Allaire G, Clerc S, Kokh S. A five-equation model for the simulation of interfaces between compressible fluids. J Comput Phys 2002;181(2):577–616.
[10] Pelanti M, Shyue KM. A mixture-energy-consistent six-equation two-phase numerical model for fluids with interfaces, cavitation and evaporation waves. J Comput Phys 2014;259:331–57.
[11] Xiao F. Large eddy simulation of liquid jet primary breakup. Loughborough University; 2012.
[12] Xiao F, Dianat M, McGuirk JJ. Large eddy simulation of single droplet and liquid jet primary breakup using a coupled level set/volume of fluid method. Atomisation and Sprays 2014;24:281–302.
[13] Tryggvason G, Scardovelli R, Zaleski S. Direct numerical simulations of gas-liquid multiphase flows. Cambridge University Press; 2011.
[14] Bnà S, Manservisi S, Scardovelli R, Yecko P, Zaleski S. Numerical integration of implicit functions for the initialization of the VOF function. Computers & Fluids 2015;113:42–52.
[15] Bnà S, Manservisi S, Scardovelli R, Yecko P, Zaleski S. Vofi — a library to initialize the volume fraction scalar field. Comput Phys Commun 2016;200:291–9.
[16] Scardovelli R, Zaleski S. Analytical relations connecting linear interfaces and volume fractions in rectangular grids. J Comput Phys 2000;164:228–37.
[17] Cervone A, Manservisi S, Scardovelli R, Zaleski S. A geometrical predictor-corrector advection scheme and its application to the volume fraction function. J Comput Phys 2009;228:406–19.
[18] Li J. Calcul d'interface affine par morceaux (piecewise linear interface calculation). C R Acad Sci Paris, série IIb, (Paris) 1995;320:391–6.
[19] Scardovelli R, Zaleski S. Interface reconstruction with least-square fit and split lagrangian-eulerian advection. Int J Numer Meth Fluids 2003;41:251–74.
[20] Weymouth GD, Yue DKP. Conservative volume-of-fluid method for free-surface simulations on cartesian-grids. J Comput Phys 2010;229(8):2853–65.
[21] Popinet S.. Basilisk; 2018. A Free-Software program for the solution of partial differential equations on adaptive Cartesian meshes; URL http://basilisk.fr.
[22] Roe PL. Some contributions to the modelling of discontinuous flows. In: Large-scale computations in fluid mechanics; 1985. p. 163–93.
[23] Brackbill J, Kothe DB, Zemach C. A continuum method for modeling surface tension. J Comput Phys 1992;100:335–54.
[24] Popinet S. An accurate adaptive solver for surface-tension-driven interfacial flows. J Comput Phys 2009;228:5838–66.
[25] Yecko P, Zaleski S, Fullana J-M. Viscous modes in two-phase mixing layers. PhysFluids 2002;14:4115–22.
[26] Boeck T, Zaleski S. Viscous versus inviscid instability of two-phase mixing layers with continuous velocity profile.. Phys Fluids 2005;17:032106.
[27] Bagué A, Fuster D, Popinet S, Scardovelli R, Zaleski S. Instability growth rate of two-phase mixing layers from a linear eigenvalue problem and an initial-value problem. Physics of Fluids 2010;22:092104.
[28] Fuster D. An energy preserving formulation for the simulation of multiphase turbulent flows. J Comput Phys 2013;235:114–28.
[29] Marcotte F, Zaleski S. Density contrast matters for drop fragmentation thresholds at low ohnesorge number. Phys Rev Fluids 2019;4(10):103604.
[30] Blumenthal R, Hoepffner J, Zaleski S. Self-similar wave produced by local perturbation of the kelvin-Helmholtz shear-layer instability. Phys Rev Lett 2011;106:104502.
[31] Clift R, Grace JR, Weber ME. Bubbles, drops and particles. New York: Academic Press; 1978.
[32] Opfer L, Roisman I, Venzmer J, Klostermann M, Tropea C. Droplet-air collision dynamics: evolution of the film thickness. Phys Rev E 2014;89(1):013023.
[33] Gunn R, Kinzer GD. The terminal velocity of fall for water droplets in stagnant air. Journal of Meteorology 1949;6(4):243–8.
[34] Dodd MS, Ferrante A. A fast pressure-correction method for incompressible two-fluid flows. J Comput Phys 2014;273:416–34.
[35] Krishnan S, Sivasamy B, Ramasamy K. Transient drag coefficients from a freely rising and falling solid sphere at moderate particle reynolds numbers. Can J Chem Eng 2016;94(5):1003–14.
[36] Rayleigh JWSL. On the capillary phenomena of jets. Proc R Soc London 1879;29:71–97.
[37] Ling Y, Fuster D, Zaleski S, Tryggvason G. Spray formation in a quasiplanar gas–liquid mixing layer at moderate density ratios: a numerical closeup. Phys Rev Fluids 2017;2(1):014005.
[38] Jain M, Prakash RS, Tomar G, Ravikrishna RV. Secondary breakup of a drop at moderate Weber numbers. In: Proc. R. Soc. A, 471, issue 2177. The Royal Society; 2015. p. 20140930.
[39] Ling Y, Zaleski S, Scardovelli R. Multiscale simulation of atomization with small droplets represented by a lagrangian point-particle model. Int J Multiphase Flow 2015;76:122–43. doi:10.1016/j.ijmultiphaseflow.2015.07.002.
[40] Matas J-P, Marty S, Cartellier A. Experimental and analytical study of the shear instability of a gas-liquid mixing layer. Phys Fluids 2011;23:094112.
[41] Eggers J, Villermaux E. Physics of liquid jets. Rep Prog Phys 2008;71:036601.
[42] Chandrasekhar S. Hydrodynamic and hydromagnetic stability. Oxford Univ Press; 1961.